PhD Dissertations and Master's Theses

12-2020

A Comparison of PID and Sliding Mode Controllers When Applied to the Orbit Raising of a Satellite Using Solar Sail Propulsion

Kayla Marie Ormiston

Follow this and additional works at: https://commons.erau.edu/edt

Part of the Mechanical Engineering Commons

A COMPARISON OF PID AND SLIDING MODE CONTROLLERS WHEN APPLIED TO
THE ORBIT RAISING OF A SATELLITE USING SOLAR SAIL PROPULSION

by

Kayla Marie Ormiston

A Thesis Submitted to the College of Engineering Department of Mechanical Engineering in
Partial Fulfillment of the Requirements for the Degree of
Master of Science in Mechanical Engineering

Embry-Riddle Aeronautical University
Daytona Beach, Florida
December 2020

A COMPARISON OF PID AND SLIDING MODE CONTROLLERS WHEN APPLIED TO THE ORBIT RAISING OF A SATELLITE USING SOLAR SAIL PROPULSION

by

Kayla Marie Ormiston

This thesis was prepared under the direction of the candidate's Thesis Committee Chair, Dr. Patrick Currier, Associate Professor, Daytona Beach Campus, and Thesis Committee Members Dr. Sergey Drakunov, Professor, Daytona Beach Campus, and Dr. Charles Reinholtz, Professor, Daytona Beach Campus, and has been approved by the Thesis Committee. It was submitted to the Department of Mechanical Engineering in partial fulfillment of the requirements for the degree of Master of Science in Mechanical Engineering

Thesis Review Committee:

_____
Patrick Currier, Ph.D.
Committee Chair

_____
Sergey Drakunov, Ph.D.
Committee Member

_____
Charles Reinholtz, Ph.D.
Committee Member

_____
Jean-Michel Dhainaut, Ph.D.
Graduate Program Chair,
Mechanical Engineering

_____
Eduardo Divo, Ph.D.
Department Chair,
Mechanical Engineering

_____
Maj Mirmirani, Ph.D.
Dean, College of Engineering

_____
Christopher Grant, Ph.D.
Associate Vice President of Academics

12/3/2020
_____
Date

Acknowledgements

I would first like to thank my thesis advisors Dr. Currier and Dr. Drakunov. Their doors were always open whenever I ran into a trouble spot or had a question about my research or writing. They consistently allowed this paper to be my own work but steered me in the right the direction whenever they thought I needed it.

I would also like to acknowledge Dr. Reinholtz as a reader of this thesis, and I am gratefully indebted to him for his very valuable comments on this thesis.

Finally, I must express my very profound gratitude to my parents and to my partner for providing me with unfailing support and continuous encouragement throughout my years of study and through the process of researching and writing this thesis. This accomplishment would not have been possible without them. Thank you.

Abstract

Researcher: Kayla Marie Ormiston

Title: A Comparison of PID and Sliding Mode Controllers When Applied to the Orbit Raising of a Satellite Using Solar Sail Propulsion

Institution: Embry-Riddle Aeronautical University

Degree: Master of Science in Mechanical Engineering

Year: 2020

Solar Sail spacecraft have become increasingly popular due to their ability to perform long term missions without the need for propellant. Because solar sail propulsion is so unique, most research has been focused on developing new mechanical control techniques. However, it can be argued that more advanced control algorithms can be used to mitigate the shortcomings of commonly used control actuators, specifically reaction wheels, when applied to solar sails. This thesis will research how a sliding mode controller compares to a PID controller with respect to settling time and state response error over a range of maximum reaction wheel torque values. The actuator saturation and actuator energy are then compared for two different sliding mode controllers and a PID controller. It was found that the sliding mode controller performed at minimum 14% better in terms of settling time and 7.7% better in terms of state response error, however the PID controller performed 24% better in terms of actuator saturation and energy. Further research should be done to study the potential benefits of sliding mode controllers in terms of their benefits to reduce actuator saturation and energy.

Table of Contents

Appendices

List of Tables

List of Figures

Chapter I:

Introduction

Back in 1865, Jules Verne wrote "there will some day appear velocities far greater than these [of the planets and the projectile], of which light or electricity will probably be the mechanical agent ... we shall one day travel to the moon, the planets, and the stars." [1]. This is theorized to be the first published work suggesting the use of light for spacecraft propulsion. Several spacecraft have used solar radiation pressure (SRP) as part of their control strategy. For example, both the Mariner 10 and MESSENGER missions took advantage of the solar radiation pressure acting on their solar panels to conserve propellant [2], [3]; MTSAT-1R uses a solar sail to counterbalance the solar radiation pressure acting on the spacecraft [4]; and after a fuel leak, the Hayabusa spacecraft used solar radiation pressure in conjunction with ion engines as an attitude control solution [5]. These spacecraft are early demonstrations of effective use of solar radiation pressure for attitude control, however several other projects have attempted active attitude control using a solar sail as their primary thrust. The most notable being the Japan Aerospace Exploration Agency's (JAXA) IKAROS project. JAXA developed a Reflectivity Control Device (RCD) that changes the reflectivity of specified sections of their sail to produce a torque, changing their sun angle and thus the direction of their thrust vector [6]. The Planetary Society also launched LightSail 2 that uses a reaction wheel for attitude control [7].

By capturing the momentum of light produced by the sun and using it as a method of propulsion, thrust is produced without the need for propellant (Figure 1).
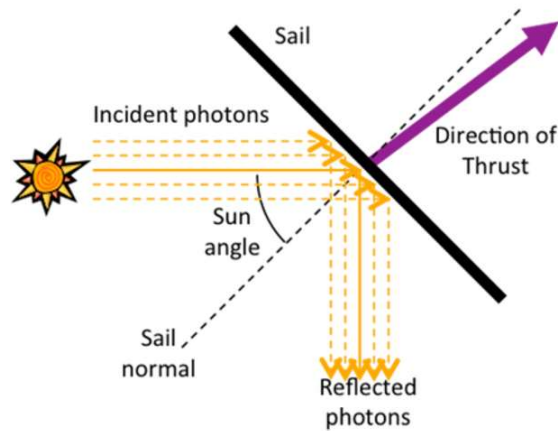
Figure 1: Illustration of how photons can be used to create thrust in space [8]

Therefore, taking advantage of the solar radiation pressure that would otherwise need to be mitigated is a more efficient propulsion method.

However, this adds considerable modifications to the attitude control system of a solar sail when compared to the typical spacecraft. Constant solar radiation pressure is acting on the sail and therefore needs to be constantly controlled in contrast to other control systems that can switch their propulsion systems on and off.

Another challenge lies in the dynamics and kinematics of a solar sail. It has been shown that small sail masses coupled with large sail areas produce the highest accelerations [8]. However, this type of sail will also produce a large moment of inertia and therefore require more torque to control. Simulations done by both Adeli and Wie show that the commonly used reaction wheel is at high risk of experiencing reaction wheel saturation to control even a small sailcraft [8] [9].

Significance of the Study

Once it is properly developed, solar sail propulsion technology will allow spacecraft to employ highly non-Keplerian orbits. One advantage of this is the potential establishment of artificial LaGrange points, allowing satellites to be placed in more useful vantage points for scientific missions such as weather observation and geoengineering [10]. Another important advantage that is gained with solar sail propulsion is the absence of fuel, which increases mission lifetimes. Because of these two main benefits, solar sail technology has many important applications for future spaceflights. A short list of possible applications includes near earth asteroid rendezvous missions, lunar base supply missions, interplanetary probing missions, solar imaging missions, and space debris deorbiting missions.

The case study used in this thesis will apply to a multi-rendezvous mission to de-orbit space debris. At altitudes above 800 km, aerodynamic drag becomes less effective, making altitudes above 800 km ideal for solar sails. Since aerodynamic drag also affects space debris, it takes longer for it to deorbit at altitude between 800-1400 km making space debris deorbiting an ideal application for solar sail technology [11].

No current systems are in place to mitigate the increase of space debris. The development of solar sail propulsion technology could allow for an autonomous system that will collect space debris around the planet. With the development of this technology, multiple spacecraft could be deployed to accomplish their missions simultaneously and remain in orbit much longer than a satellite with traditional propulsion attitude control. From this research, steps will be made to reduce the amount of space debris, resulting in fewer subsequent collisions.

Even though extensive international guidelines have been released on how to mitigate space debris, such as ISO 24113, these guidelines are non-binding [12]. Since 1961, over 290 events have occurred that contributed to the increase in space debris. It is assumed that 750,000 objects larger than 1 cm have been produced as a result [11]. The largest debris-generating event being the Chinese FengYun-1C , an intentional anti-satellite missile test, which increased the collision probability by 60% for spacecraft in sun-synchronous orbit [13]. Because these objects have such high velocities, small objects have the potential to cause major damage. Kessler Syndrome is the scenario postulated by Don Kessler in 1978 theorizing that fragments will continually collide with large objects until all that is remaining is collision fragments. As stated previously, most space debris is trapped orbiting at altitudes between 800-1400 km, therefore making it a perfect area for Kessler Syndrome to occur. It is estimated that an object as small as 1 mm could destroy subsystems on a satellite, a 1 cm object can penetrate the ISS shields, and collision with a 10 cm object can cause catastrophic fragmentation [14]. Without mitigation, altitudes from 800-1400 km may be considered too dangerous for space activities within a few decades, posing challenges to many valuable scientific missions.

Figure 2: Comparison of space debris from 1957-2018 with a projection for 2030 [47]

Figure 2 is NASA's prediction of what space debris could look like in 2030 compared to previous years if there is no mitigation.

Statement of the Problem

Changing the direction of a solar sail's normal vector requires a larger amount of torque than a typical satellite due to the increased moment of inertia caused by the sail. Because of this, many researchers attempt to provide new control actuator solutions that work more effectively for solar sails. However, these solutions often prove to be mechanically complex with many points of potential failure. Using these new control methods also makes it difficult to reach the required Technological Readiness Level (TRL) to launch a solar sail mission. Without a high enough TRL, missions will not make it to launch until extensive testing is performed. This would significantly increases the timeline on solar sail projects and hinder the progress that can be made with solar sail technology. It can be argued that rather than changing the control actuators, improving the control algorithm will allow reliable and well-studied control actuators, such as reaction wheels, to be used. However, solar sail research that is focused on the control algorithm often employs algorithms with major limitations.

As discussed in more detail in Chapter II, extensive research has been done on PID algorithms and LQR algorithms. While these algorithms are proven to work in numerical simulations, they require fine tuning that cannot be accurately achieved through simulation. A more robust solution would be the sliding mode controller (SMC). Since the sliding mode controller switches between the minimum and maximum torques values, it is not as sensitive to controller gains as PID and LQR controllers. This also makes the sliding mode controller more directly correlated to electrically switching actuators, potentially improving actuator performance in comparison to PID and LQR controllers. Research assessing the benefits of SMC is also discussed in Chapter II.

Purpose Statement

      The purpose of this thesis is to explore the advantages of more advanced control algorithms when applied to solar sail technology.

Research Questions

· Will a sliding mode controller show improved performance compared to a PID controller in regard to settling time and state response error over a range of maximum torque values?

· When using a constant maximum torque value, will the SMC also show improved performance compared to a PID controller in terms of actuation energy and state response error?

Delimitations

      In order to reduce the amount of complexity to an already complex system, the well-studied, cost-effective reaction wheels will be used for attitude control. This thesis will provide simulations that model the solar sail dynamics and kinematics. A non-linear sliding mode controller is derived and applied to the attitude of the solar sail spacecraft. A PID controller will also be developed for comparison. This simulation will study the systems state response from each controller for a varying maximum torque values to analyze the performance of different sized reaction wheels. An in-depth performance analysis will then be done with the lowest maximum torque value based on actuator saturation and actuation energy.

      This thesis models a solar sail in an initially circular, equatorial orbit with an initial altitude of 1800km. A PID controller is initially developed to compare its state response error and settling time to the system with that of the sliding mode controller's state response. The PID controller will have saturation limits based on the maximum torque values used. The sliding mode controller is non-linear, and Lyapunov stability is mathematically proven for the given

system. To mitigate the prospect of gimbal lock, the spacecraft's attitude kinematics will be modeled with quaternions.

It will be assumed that the solar sail will use reaction wheels as the primary control mechanism. The spacecraft will feature of 40x40 m sail, resulting in a characteristic acceleration of $2.87 * 10^{-4} \frac{m}{s^2}$. A CubeSat will serve as the base of the spacecraft. The mass of the spacecraft is 40 kg. It will also be assumed that the spacecraft is in a circular orbit upon launch from the rocket. The sailcraft will perform two 90-degree roll rotations in one orbit to perform orbit raising. This is discussed in more detail in the following chapters.

Limitations

The solar sail model assumes a rigid body spacecraft using an ideal sail model. Therefore, this research will not model sail wrinkles, sail billowing, thermal deformation of the sail, or structural vibration of the sail. These effects are complex to calculate and predict and out of scope of this thesis [15].

Aerodynamic drag will also not be modeled. The altitude of the initial orbit has negligible aerodynamic drag forces [11]. Effects due to Earth's oblateness also have minimal effect on equatorial orbits [15].

List of Acronyms

ACS	Attitude Control System
AD	Aerodynamic Drag
AMT	Active Mass Translator
CM/CP	Center of Mass/Center of Pressure

LEO   Low-Earth Orbit

RCS   Reaction Control System

RSLQR   Robust Servomechanism Linear Quadratic Regulator

RW   Reaction Wheel

SLS   Space Launch System

SRP   Solar Radiation Pressure

TRL   Technological Readiness Level

List of Units

AU   Astronomical Unit

mNm   Milinewton-Meter

J   Joules

rad   Radians

s   Seconds

Chapter II:

Literature Review

Solar Sail Projects

Several solar sail projects have been lost in launch failures, such as NASA's NanoSail-D (2008) and The Planetary Societies' Cosmos I (2005) [16], [7]. Before NASA or The Planetary Society could try again, JAXA launched IKAROS in 2010. They ambitiously launched the world's first interplanetary solar sail to Venus. IKAROS became the first successful spacecraft fully propelled by sunlight [6]. Three years after NanoSail-D, NASA launched NanoSail-D2 to test sail deployment and de-orbit capability in order to raise the Technological Readiness Level (TRL) of solar sails. Active attitude control was not attempted for this mission [17]. In 2015, The Planetary Society launched LightSail 1 to demonstrate a new sail deployment method. This system did not perform solar sailing, and therefore had no controls for solar sailing [7]. However, in 2019, LightSail 2 launched. That spacecraft was able to successfully raise its orbit with a solar sail, although one-third of the time it is in detumble mode due to momentum wheel saturation [18]. To learn from past projects, the ones that had attitude control systems will be analyzed in depth.

While it is clear that not many solar sail projects have come to fruition, there have been several promising projects proposed and currently being developed that will also be discussed. NASA's Near-Earth Asteroid (NEA) Scout project is planned to launch as a secondary payload on board the Space Launch System (SLS) Artemis-1 launch, scheduled for March 1, 2021. Its mission is to rendezvous with a nearby asteroid to conduct science imagery. Another promising project is the University of Illinois' CubeSail project. CubeSail is a proposed low-cost

demonstration of UltraSail, a larger, heliogyro concept meant for interplanetary and interstellar missions [19]. For the CubeSail demonstration, two nearly identical CubeSat satellites are to deploy a $20m^2$ sail. The two satellites will be inserted into a sun-synchronous terminator orbit at an altitude of 800km [20]. The University of Surrey also has a project named CubeSail that is a 3U CubeSat with a 25 m^2 sail intended to demonstrate the propulsive effect and deorbiting capabilities of solar radiation pressure [21].

Even though these projects have vastly different missions, the control algorithms used are mainly PID's and LQR's with a few outliers. These algorithms will be discussed in more detail in the following sections.

PID Controllers

As mentioned in Chapter I, PID controllers work well in simulation, but there are limitations that limit their effectiveness in real-world scenarios if those limitations are not addressed. The Planetary Society proved this results in 2019. As shown in Figure 3, the simulated data does not align well with the flight data. In an interview, Project Manager David Spencer admitted they are actively controlling the spacecraft two-thirds of the time. However, one-third of the time they are in detumble mode due to the inability to get rid of the momentum produced by the momentum wheel [18]. To learn from their mistakes, the modeling and controls of LightSail 2 will be analyzed.

Boreal Space modeled the initial controllers used on LightSail 2. They modeled aerodynamic drag, solar radiation pressure, gravity gradient, and several sensor errors to

construct a PID controller for detumbling. Georgia Institute of Technology then modeled the

apogee raising strategy with an on/off control strategy (Figure 4).

Figure 3: Flight data and sail control performance for LightSail 2 [18]
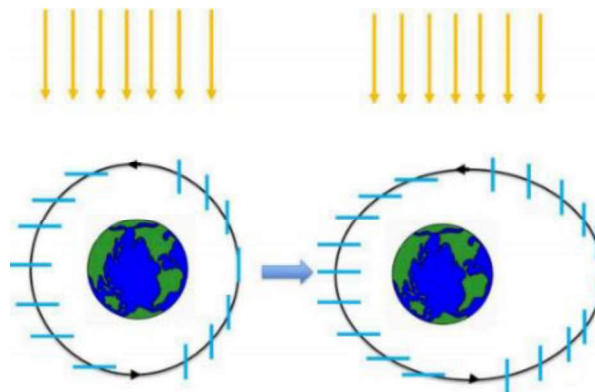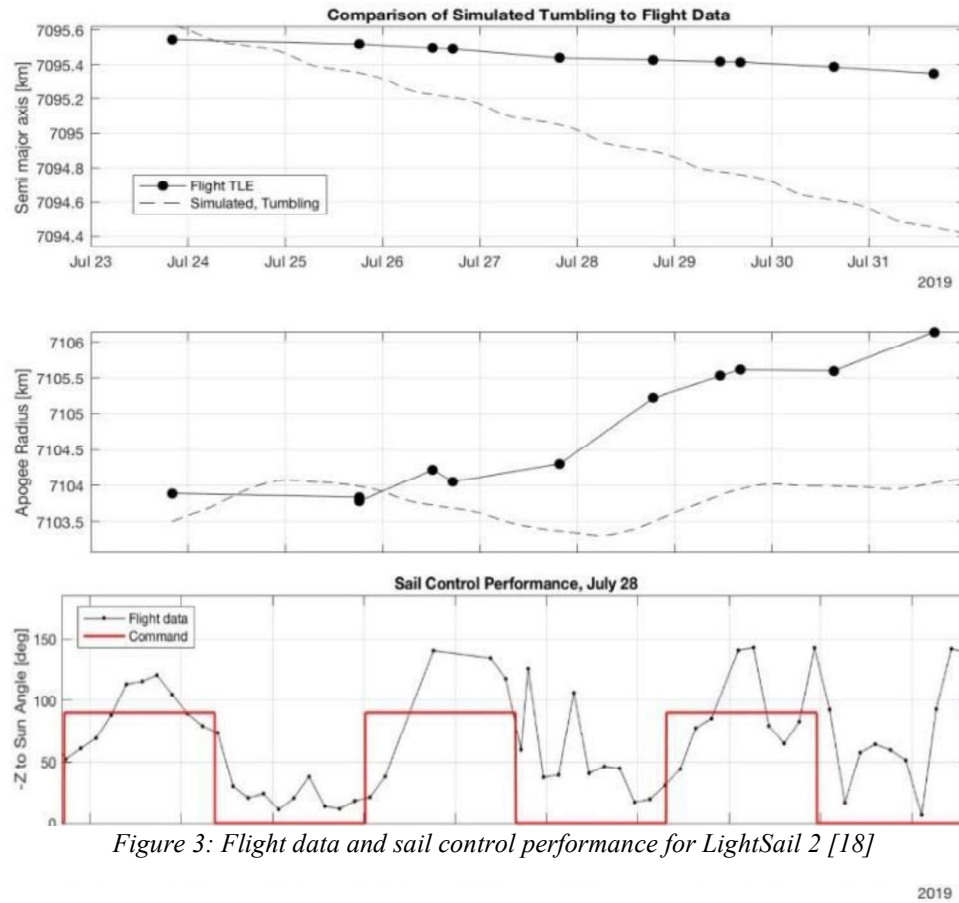
Figure 4: On/ off control strategy attempted by LightSail 2 [22]

The results from this simulation are shown in Figure 5.
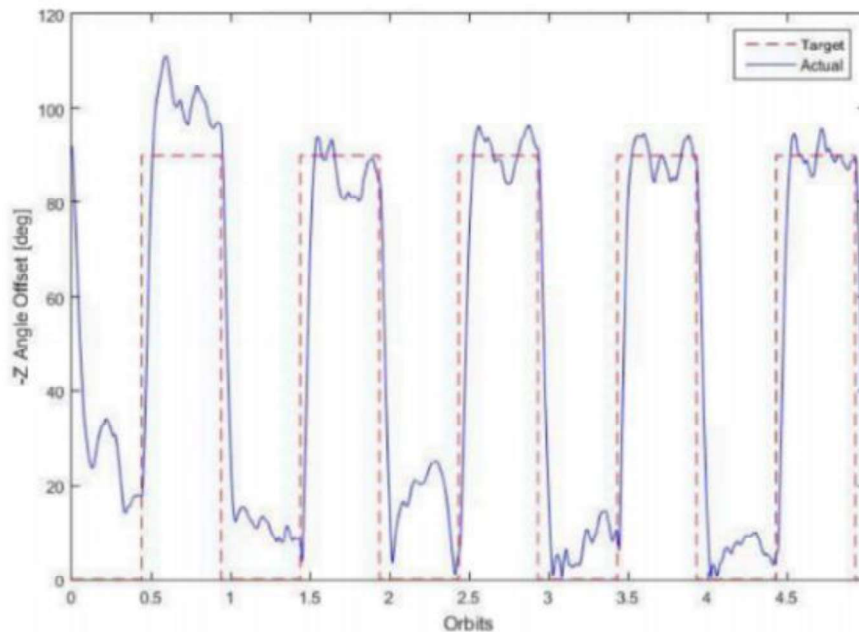
Figure 5: Simulation results from LightSail 2 control strategy [22]

This figure shows that the simulation results of their control algorithm proved to be successful, however as Figure 3 shows, the real-world results were not as successful. Even though their model was thorough enough to include AD, gravity gradient, and SRP, they did not provide any alteration to the controller gains outside of their simulations [22].

While this algorithm was implemented in the on-board controller, manual control of the algorithm parameters and spacecraft actuators was also available. This decision proved to be very useful when LightSail 2's momentum wheel became saturated. The team resorted to manual control to switch the spacecraft into detumbling mode. However, the team added a new control mode that abandons the on/off strategy. They now keep the spacecraft sun-pointed to reduce momentum wheel saturation and to provide a better charging orientation for the batteries [23]. While this control strategy will not reduce orbital decay, it could offer a more consistent initial attitude for starting on-off thrust maneuvers

Two proposed improvement to this method comes from the University of Surrey. Specifically, Nadir Adeli's dissertation on attitude control and deployment provides several improvements to the simple PID algorithm (2011).

One improvement is a simple quaternion feedback proportional derivative (PD) controller. By inputting the spacecraft's orientation, angular velocity with the commanded angular velocity and quaternion profile, the PD controller outputs a torque command about each axis from equation 2.1.

$$u = -Kq_e - C\omega \qquad (2.1)$$

Where q_e can be found from equation 2.2.

$$\begin{bmatrix} q_{1e} \\ q_{2e} \\ q_{3e} \\ q_{4e} \end{bmatrix} = \frac{1}{2} \begin{bmatrix} q_{4c} & q_{3c} & -q_{2c} & -q_{1c} \\ -q_{3c} & q_{4c} & q_{1c} & -q_{2c} \\ q_{2c} & -q_{1c} & q_{4c} & -q_{3c} \\ q_{1c} & q_{2c} & q_{3c} & q_{4c} \end{bmatrix} \begin{bmatrix} q_1 \\ q_2 \\ q_3 \\ q_4 \end{bmatrix} \qquad (2.2)$$

And K and C are quaternion error and angular velocity error gains. For the problem to be considered globally asymptotically stable, equations 2.3-2.6 show possible K and C combinations that can be used.

$$[K = kI, \qquad C = diag(c1, c2, c3)] \qquad (2.3)$$

$$\left[K = \left(\frac{k}{q_4^3} \right) I, \qquad C = diag(c1, c2, c3) \right] \qquad (2.4)$$

$$[K = ksgn(q_4)I, \qquad C = diag(c1, c2, c3)] \qquad (2.5)$$

$$[K = (\alpha J + \beta I)^{-1}, \qquad C = diag(c1, c2, c3)] \qquad (2.6)$$

Where k, c_i, α, and β are positive scalar constant, I is the identity matrix, and sgn() represents the signum function.

Another control method proposed by Adeli is a PID controller with saturation limiters (2010). The definition of the control output is given in equation 2.7

$$u = -sat_u\{Ksat_L(e) + C\omega\} \tag{2.7}$$

Where K is the attitude gain, C is the attitude rate gain, U is the torque limitation on the actuators, and L is a limit on the error. To avoid actuator saturation, as happened to LightSail 2, K and C should be defined as $K = \omega_n^2 J$ and $C = 2\zeta\omega J$ where ω_n is the linear control bandwidth and ζ is the damping ratio. To further improve the controller by eliminating steady-state error, an integral term must be added. Also, to reach a more rapid transient settling, L can be defined using equation 2.9, resulting in the final PID controller:

$$u = -sat_u\{Ksat_L\left(e + \frac{1}{T}\int e\right) + C \tag{2.8}$$

$$L = \frac{C}{K}\min\left\{\sqrt{4a|e|}, |\omega|_{max}\right\} \tag{2.9}$$

$$a = \frac{U}{J} \tag{2.10}$$

Where T is the time constant controlling the integral term (typically $T \sim 10/(\zeta\omega_n)$) [8]. While this controller solves the problem of control hardware limitations, it is vulnerable to hardware malfunction. However, that is where NASA's control algorithm for their NEA-Scout project excels.

Orphee, et al. at NASA proposes using three subsystems for their Attitude Control System (ACS), the Reaction Wheel (RW) control system, the Reaction Control System (RCS), and an Active Mass Translator (AMT) (2017). By using four reaction wheels, the team will use an allocation algorithm that will distribute the commanded torque to prevent reaction wheel saturation, taking care of the main hardware limitation of reaction wheels Figure 6 shows the feedback control loop for the reaction wheel.
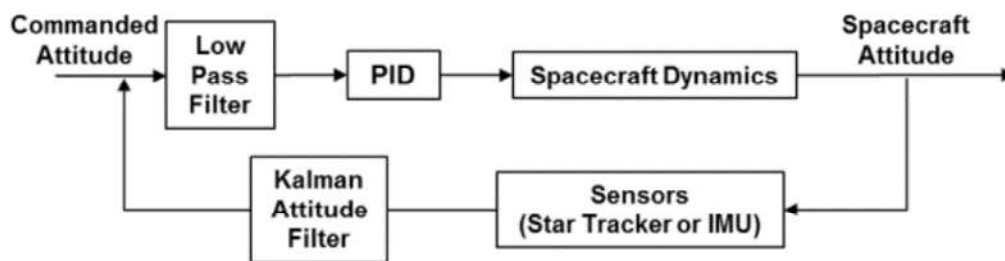
Figure 6: Feedback control loop for NEA-Scout's reaction wheel [37]

As shown, the star tracker and IMU sensors are input to a Kalman filter. This is necessary because of the varying amounts of noise experienced by the star tracker and IMU at different body rates.

a.)   b.)

c.)
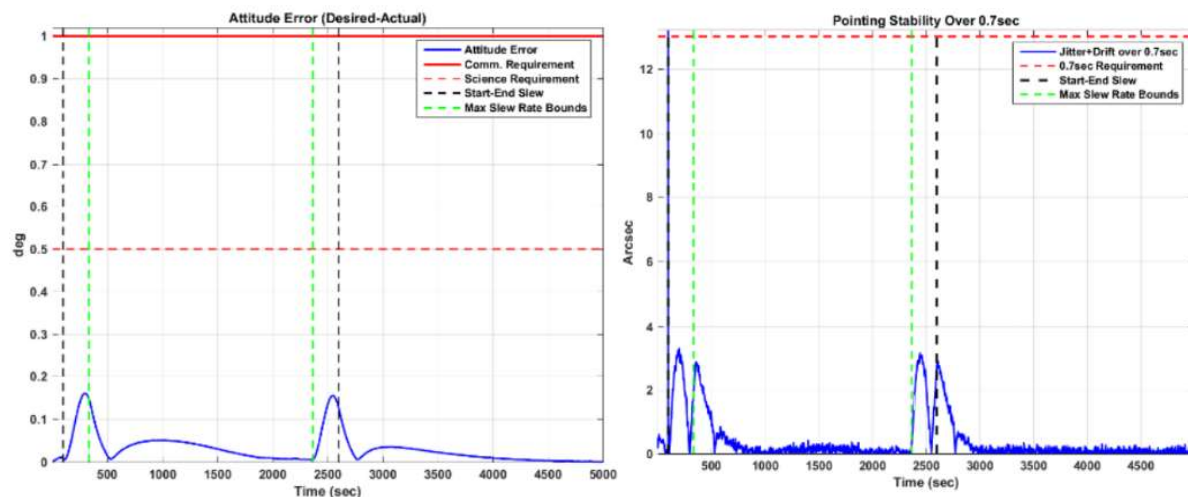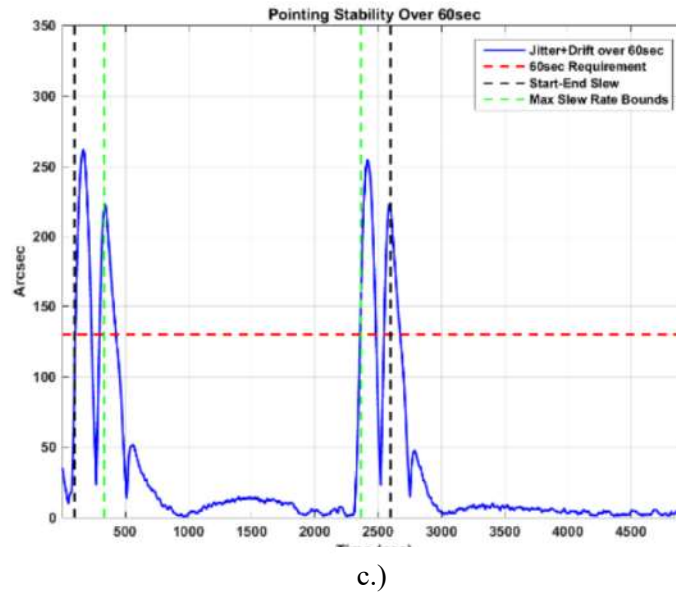
Figure 7: Simulations results in terms of attitude error (left), pointing stability over 0.7 seconds (middle), and pointing stability over 60 seconds (right) for NEA-Scout's reaction wheel control feedback loop [37]

Using a Kalman filter is also useful in the case of sensor failure. This algorithm was able to meet NASA's control requirements of 0.5 degree pointing attitude error, a maximum of 130 arcsec error during a 60 second period, and a maximum of 13 arcsec during a 0.7 second period. The results of the simulation are shown in Figure 7.

LQR Controllers

Unlike a PID controller, the LQR controller provides optimal control, though it does come with the cost of added complexity. Like the PID controller, the LQR gains are difficult to tune properly through simulation. This is due to both environmental uncertainties, and, unlike PID controllers, the non-intuitive relationship between the controller parameters and the controller behavior. One proposed solution comes from Tsinghua University.

Shahin Firuzi and Shengping Gong (2018) propose using a robust servomechanism linear quadratic regulator (RSLQR) for the control algorithm for a flexible solar sail in Low-Earth Orbit (LEO). This algorithm uses an LQR controller that is augmented with a model of the actuator dynamics. Including the actuator dynamics improves the model of the environment, allowing the controller to better handle environmental uncertainties. In the paper, they model solar radiation pressure and aerodynamic drag. They then analyze the deformation under these forces and recalculate the resulting torques accordingly. It is assumed that sliding masses will be used to change the CM/CP offset of the spacecraft for attitude control. Given the model of the system as $\dot{z} = Az + Bu$, the control law is defined as $u = -K_c z$ where u is the control input vector, z is the state vector, and K_c is the total gain. K_c can be found from solving the equation $K_c = R^{-1}B^T X$ where R is a symmetric, positive definite cost matrix, B is taken from the system model, and X is solved from the Riccati equation shown in equation 2.11.

$$XA + A^T X - XBR^{-1}B^T X + Q = 0 \qquad (2.11)$$

Where Q is a symmetric, positive semidefinite cost matrix. The simulation modeled a circular orbit at an altitude of 600km and 20kg sliding masses. The results from this simulation are shown in Figure 8.
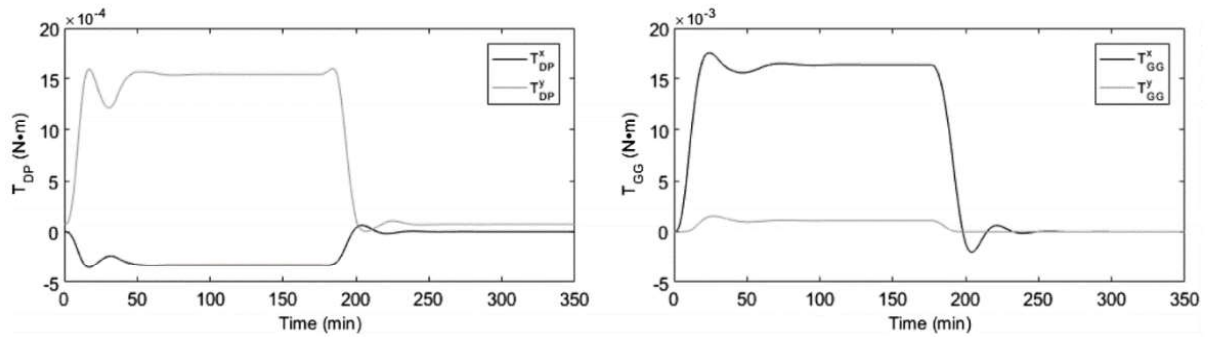
Figure 8: Simulation results of circular orbit at 600km including SRP of flexible sail, aerodynamic drag, and RSLQR controller where T_{Dp} is the torque vector generated by deviation of center of pressure, and its component
[38]

While this helps with the problem of environmental uncertainty, the problem of tuning the complex controller gains still exists. Pukniel, Coverstone, Burton, & Carroll from the University of Illinois attempts to solve this problem (2011). The University of Illinois' optimal LQR attitude control simulator is shown in Figure 9.
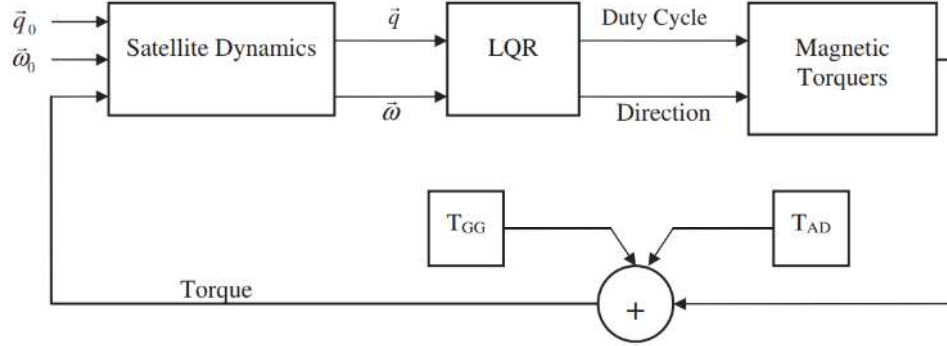
Figure 9: CubeSail's attitude control simulator diagram where $\vec{q}_0$ is the initial attitude, $\vec{\omega}_0$ is the initial rotational rate, T_{GG} is the gravity gradient torque, and T_{AD} is the aerodynamic drag torque [20]

Their attitude control simulator, shown in Figure 9, outputs the optimum duty cycle to detumble and orient the satellite from the linear quadratic regular (LQR) block. The LQR uses two cost functions, detumbling time and tracking time, that are changed based on the phase of the mission. Initially, the controller is meant to focus on reducing the rotation rates, therefore the detumbling time cost function is defined as the time required to reach $0.1^{\circ}/s$ on all three axis. After this has been achieved, the tracking time cost function is used. To focus on proper alignment of the satellite, this cost function is defined as the time required to stabilize the spacecraft within 5° on all three axes.

Because tuning LQR parameters is often non-intuitive, the CubeSail team decided to tune their controller using a genetic algorithm. They run the algorithm for 50 generations and test the

attitude control simulator with random initial altitudes and worst-case rotational rates 1000

times. The results from this simulation are shown in Figure 10.
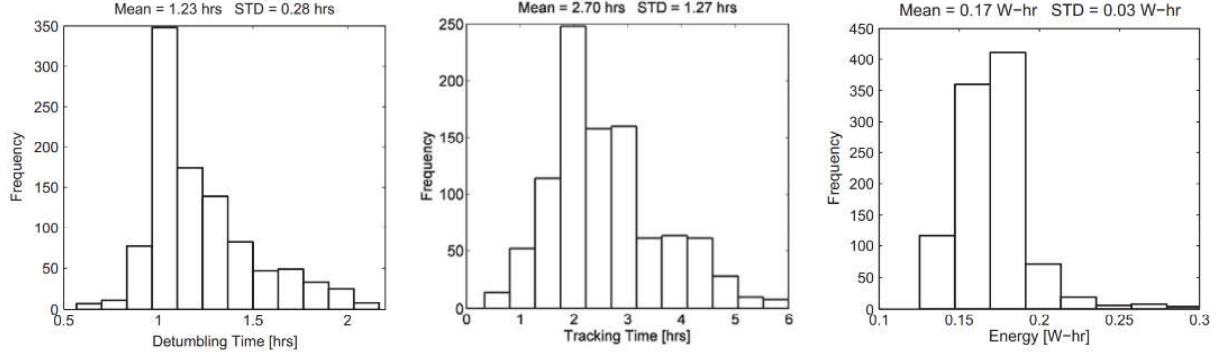
Figure 10: Statistical aggregation of the detumbling time, tracking time, and energy when run 1000 times [20]

Since generic algorithms are probability based, the results shown in Figure 10 show a

well-distributed curve. Therefore, the most frequently output performance is average rather than

optimal. While this method may be more robust to uncertainties, it comes at a cost of losing

optimality.

SMC

Sliding mode controllers are known to be more robust in comparison to both PID and

LQR controllers, especially in their ability to remain stable in the case of unpredictable

conditions. For example, Lian et. al analyze the effects of actuator saturation and model

uncertainty when using a SMC for solar sail attitude control [24]. For this controller, Lian et. al

uses a radial basis function (RBF) to approximate the upper bound of the unknown model

uncertainty caused by elastic deformation of the structure and the input error between the actual

and unrestricted control inputs. They derive the linear sliding mode function in equation 2.12.

$$s = ce + Me'$$ (2.12)

Where e is the error between the actual and desired attitude angle and e' is its derivative, c is the controller gain, and $M = \frac{\sqrt{\mu\rho}}{R^2}$ where μ is the gravitational constant, ρ is the difference between the actual control input and the unrestricted control input and R is the position vector. A saturation function is then applied to the SMC function to reduce chattering. Using the Lyapunov stability theorem, the system is proven to be asymptotically stable when the true anomaly is ∞. This paper also proves the system has finite true anomaly stability. The authors also designed bang-bang radial basis function controller for comparison. The results of their numerical simulations are shown in Figure 11.
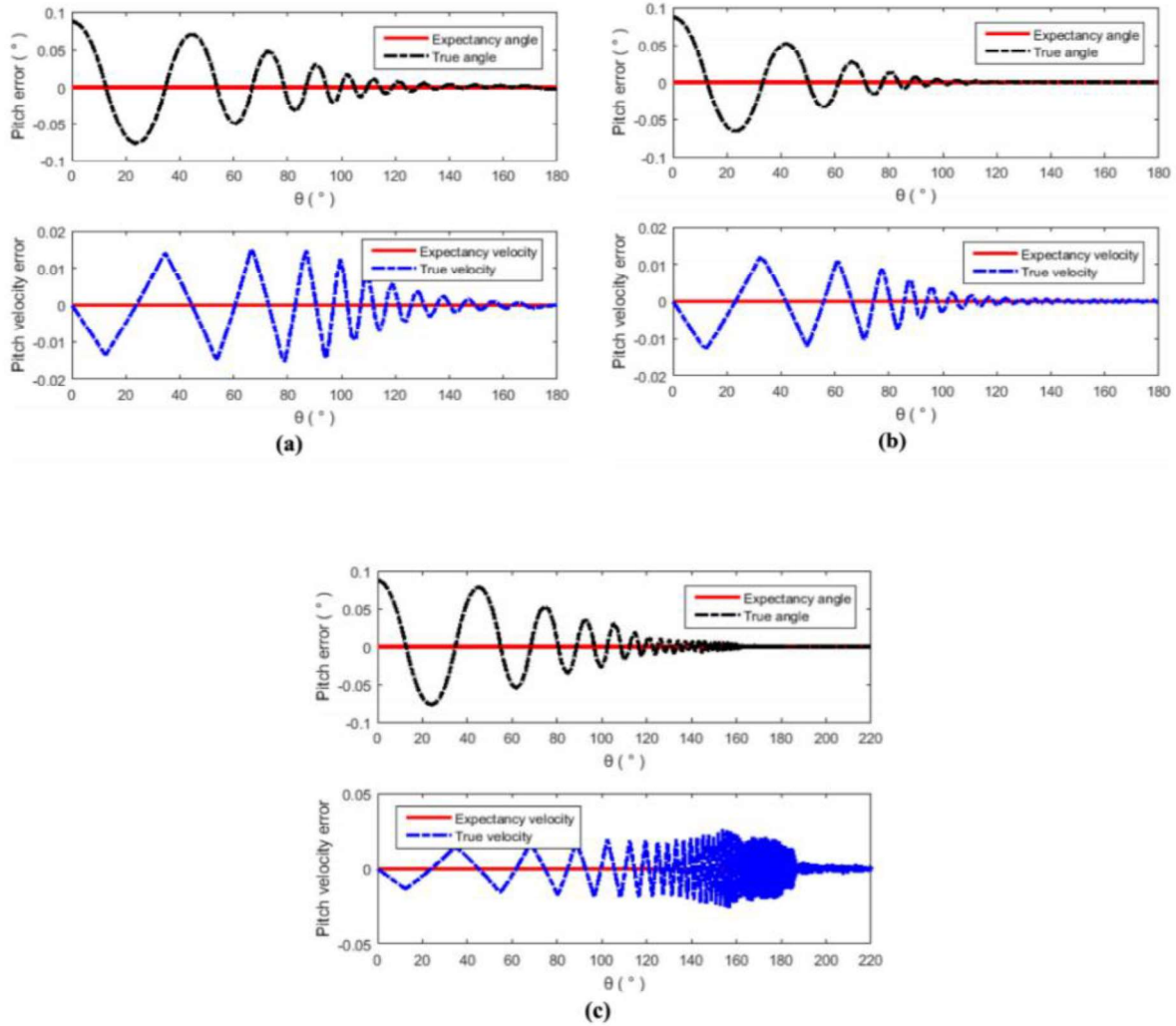
Figure 11: Pitch and pitch velocity error results for a) infinite-time asymptotic stable control; b) finite-time asymptotic stable control; c) bang-bang-RBF control [24]

As shown, the SMC with finite-time asymptotic stability had the lowest state response error and shortest transition time, making it the best performing controller. To further test the controller, an attitude maneuver from earth-to-sun pointing mode is simulated. The results are shown in Figure 12.
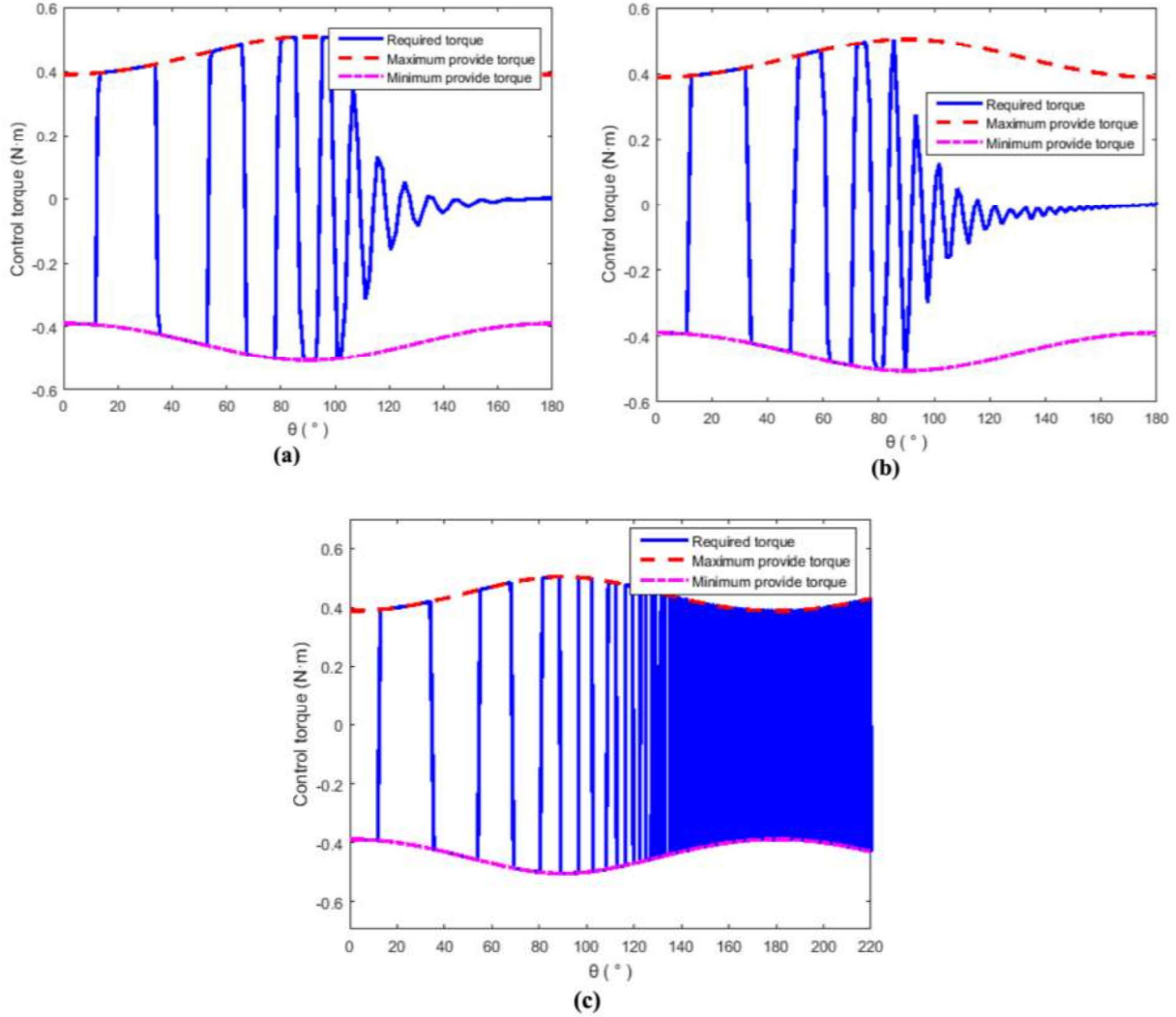
Figure 12: Control torque results for a) infinite-time asymptotic stable control; b) finite-time asymptotic stable control; c) bang-bang-RBF control [24]

As shown, the SMC with finite-time asymptotic stability again proved to perform the best based on state response error and transition time criteria.

While this study using sliding mode control is valid, research has made improvements to the use of the sliding mode control function with solar sail applications. One such used an adaptive second-order SMC to analyze station-keeping control in a displaced orbit for a solar sail. Due to its variable structure, the second-order SMC has improved robustness. It can also deal with nonlinear and nonaffine systems. [25]

In this thesis, a second-order terminal sliding surface is adopted. A control law is then derived using more reasonable uncertainty variables, such as lightness number and external disturbances. An adaptive law is derived for these two variables and updated separately for the control law. To reduce the potentially large errors caused by taking the first and second derivative of the sailcraft's position, a high-gain observer is also constructed. The response curves from the numerical simulations, assuming initial injection errors of the displaced radius and height error are both 10000 km, are shown in Figure 13.
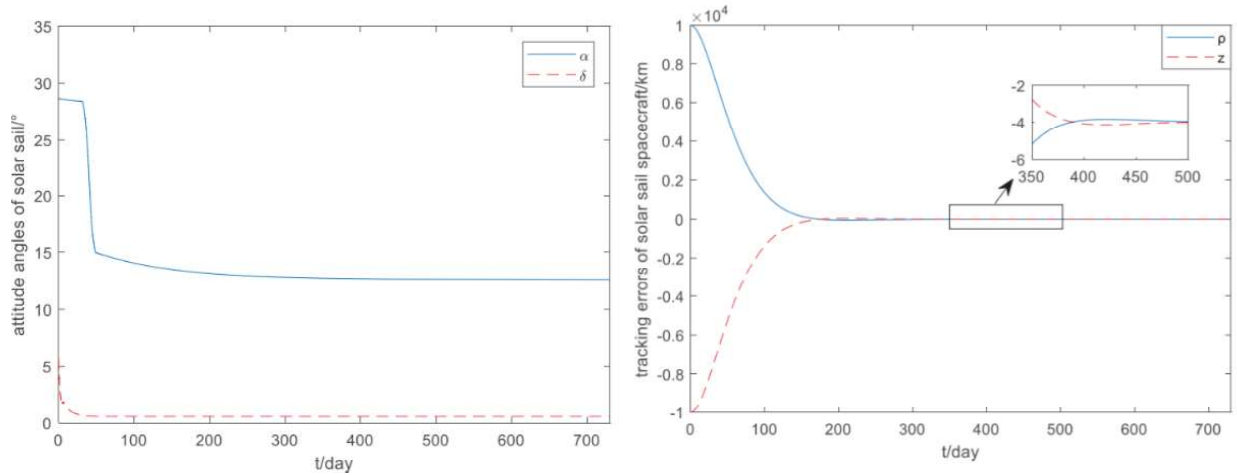
Figure 13: Tracking error response and attitude angles of the solar sail [25]

As shown, the attitude is stable, and it lacks the common chattering problem with SMC. Even with the initial errors, tracking error converge to less than 6 km after 350 days. With this method, only the spacecraft position is needed, eliminating the need for velocity or accelerating. While

this controller is more advance and therefore show impressive results, the actuator is ignored and therefore so is the potential for actuator faults.

Other Controllers

Another noteworthy control strategy is the one developed by Tsuda used on the IKAROS project (2010). IKAROS was the first spacecraft to truly demonstrate solar sailing, and active attitude control. Because it was an interplanetary mission, the sail for IKAROS is much larger than most of the other sails at 200 m^2 JAXA developed a Reflectance Control Device (RCD) for their sail. These devices consist of a liquid crystal that changes its reflectivity upon an electrical impulse. IKAROS used 72 sheets of RCDs, shown in Figure 14, allowing them to change the spin axis orientation by 1 degree at 1 AU at 1 rpm spin rate.
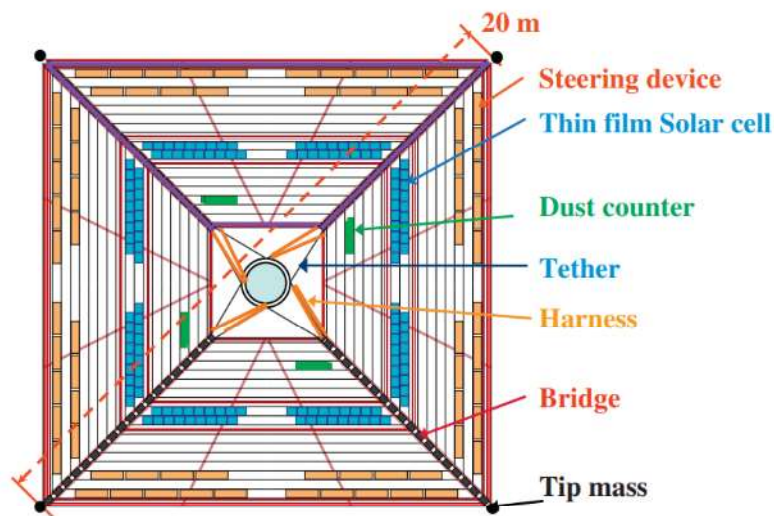
Figure 14: IKAROS sail design [6]

JAXA did not use booms to deploy their sail, instead they attached weights to the end of tethers and use gas-liquid thrusters to spin the spacecraft and keep the sail deployed. Due to their

unique control and deployment methods, their control strategy is highly specific to their

spacecraft. While this may not be applicable to most spacecraft, because IKAROS was the most

successful solar sail project to date, an analysis of their control strategy is beneficial.

Since their sail is constantly spinning, they only use the Sun angle to control their

attitude, as shown in Figure 15.
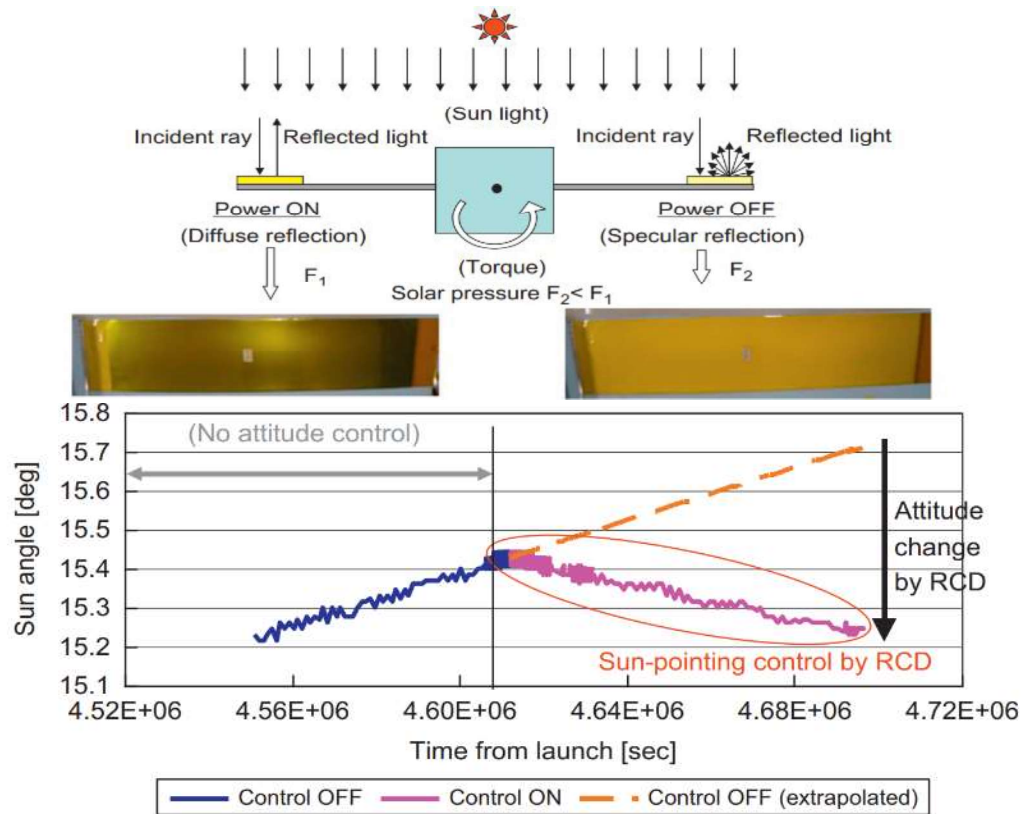
Figure 15: IKAROS Control Strategy

The results of JAXA's control strategy is also shown in Figure 15. As shown, they can

dramatically change their Sun angle, which directly correlates to the thrust produced. On

December 8, 2010, IKAROS successfully completed the Venus flyby, thereby completing all

their mission objectives [6].

Because IKAROS is a spin-type solar sail, its attitude control logic is slightly more complicated. The RCD's must be switched on and off in synchronization with the spin motion in order to maintain attitude control in a fixed direction (Figure 16).
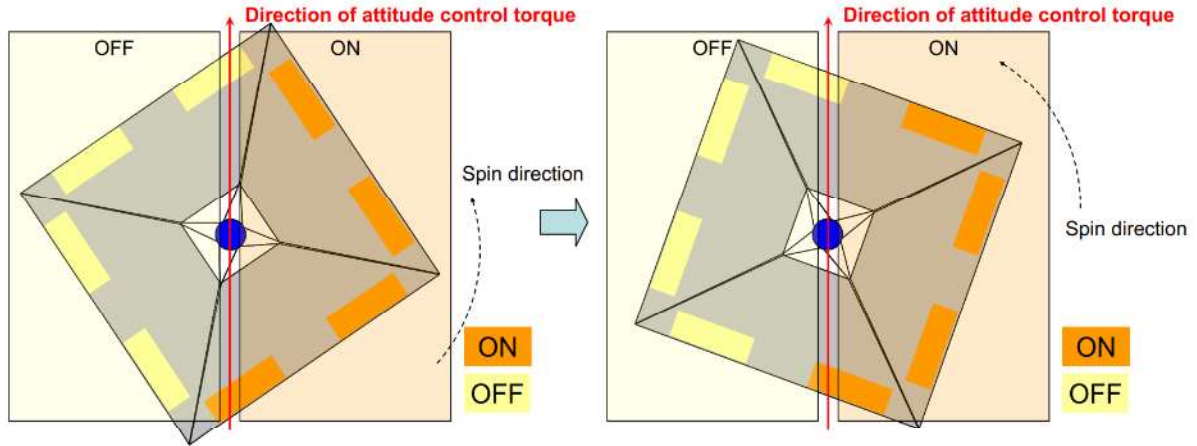
Figure 16: Demonstration of IKAROS control logic for RCD [6]

The control logic for this system requires the onboard controller to receive a pulse signal from a slit-type sun sensor during every rotation. From the pulse signal, the spin period is calculated and used to switch the RCD's on and off [26].

Summary

It can be concluded that PID controllers are widely used due to their simplicity. However, an argument can be made that using a PID controller without modifications to the controller gains or accounting for hardware limitations is not enough for a solar sail project, as demonstrated with LightSail 2. An LQR controller may provide more robust control, however the same problem persists with environmental uncertainties leading to ineffective controller parameters. LQR controllers have an additional complication of tuning non-intuitive controller parameters. While this can be solved using genetic algorithms, the nature of this method of

artificial intelligence not only greatly increases computational complexity, but also provides average gains and often overlooks simpler solutions. The best controller that is analyzed in this thesis to solve the problem of uncertainties and actuator dynamics is the SMC. Based on the benefits proven from previous research, it can be argued that SMC deserves more research into improving the control law to analyze reaction wheel saturation for solar sail attitude dynamics control. One method is described in detail in the next chapter.

Chapter III:

Methodology

Research Approach

a.) Research Question

This thesis attempts to answer the following research questions:

· Will a sliding mode controller show improved performance compared to a PID

controller in regard to settling time and state response error over a range of maximum

torque values?

· When using a constant maximum torque value, will the SMC also show improved

performance compared to a PID controller in terms of actuation energy and state

response error?

b.) Data Collection

To answer the research questions posed, the attitude quaternions for both the PID

controller and the SMC will be calculated from an orbital and attitude dynamics and

kinematics simulation algorithm and analyzed based on their output torque, stability, and

settling time.

c.) Ideal Outcome

To successfully answer "yes" to the research questions posed, the SMC must show

improved state response error and shorter settling time than a PID controller. The actuation

energy and state response error must also be lower.

Mathematical Model

a.) Discussion of Simulation

To analyze the response of each controller with different reaction wheels, a range of maximum reaction wheel torque values are tested on each controller. As the maximum torque value decreases, the likelihood of reaction wheel saturation increases because there is less torque available to stabilize the system. Therefore, maximum torque values ranging from 10 mNm (typically seen on 6-12 U CubeSat's) to 0.2 mNm (typically seen on 1-3 U CubeSat's) are tested [27] [28]. The controller gains will be tuned to produce the lowest settling time for each maximum torque value. Since the roll angle is defined as normal to the sail, and the angle between the sail normal and the direction of the solar radiation pressure force is directly related the amount of thrust that will be produced, only the settling time for the roll angle is analyzed. This is shown in Figure 19 The controller performance is then compared for a constant maximum torque value using settling time, state response error, and actuator energy. Settling time is calculated by subtracting the time at which the roll axis first reaches zero by the time the roll axis from the controller is within 2% of zero. State response error is calculated by taking the difference between the actual attitude quaternion and the desired attitude quaternion for each time step, finding the sum, and normalizing over the simulation runtime. Actuation energy is calculated by integrating over the output torque curve. All simulations were done in MATLAB with a time step of 0.1s.

The physical characteristics of the sail are taken from a proposed sail design used in Bong Wie's textbook [29]. The area of the sail (A) is $1400m^2$, the total mass (m) is $40kg$, and the moments of inertia are $J_1 = 6000kg \cdot m^2$, $J_2 = 3000 \ kg \cdot m^2$, and $J_3 = 3000kg \cdot m^2$ where 1, 2,

and 3 represent the roll, pitch, and yaw angles respectively. Using these values, the characteristic acceleration can be calculated from equation 3.1

$$a_c = \frac{\eta P A}{m}$$
(3.1)

Where $P = 4.563 * 10^{-6} \frac{N}{m^2}$ is the nominal solar-radiation-pressure constant at 1 AU from the sun and η is the overall sail thrust coefficient, typically around 1.8 [29]. This results in a characteristic acceleration equal to $2.87 * 10^{-4} \frac{m}{s^2}$.

The steering laws for the solar sail involve two 90-degree yaw rotations of the body frame throughout the orbit to demonstrate orbit raising. A schematic is shown in Figure 19.
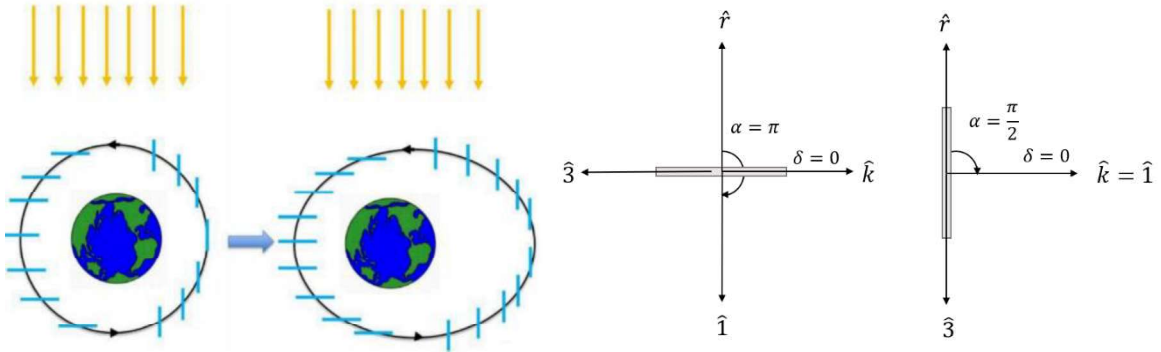
Figure 19: Demonstration of orbit raising logic using two 90-degree yaw rotations (left) [22] with the steering angles used shown in both the orbital reference frame $\{\hat{r}, \hat{\theta}, \hat{k}\}$ and body reference frame $\{\hat{1}, \hat{2}, \hat{3}\}$ (right).

This is the same steering logic used by LightSail 2, which resulted in actuator saturation using a PID controller. Using this logic with attitude quaternions and the mathematical model presented earlier in the chapter, the resulting attitude quaternion is potted in Figure 20.
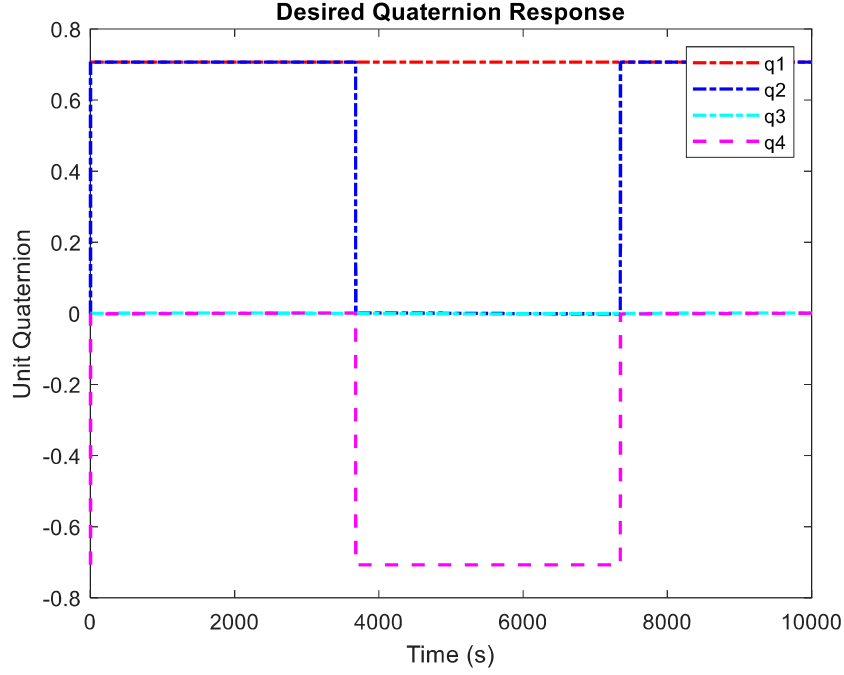
Figure 20: Desired quaternion response using two 90-degree rotations

b.) Attitude Dynamics and Kinematics

The basic attitude dynamics of a rigid body spacecraft is shown in equation 3.2.

$$J\dot{\omega} = \omega \times J\omega + \tau_{SRP} + \tau_{RW} \tag{3.2}$$

In these equations, ω is the state vector consisting of the roll, pitch and yaw angles. J is the moment of inertia vector. τ_{SRP} is the torque due to solar radiation pressure, and τ_{RW} is the torque produced by the reaction wheel. Here, the reaction wheel dynamics are estimated as $\dot{h} = -\tau_{RW}$, where h is the angular momentum of the reaction wheel.

A study by Bong Wie shows that defining control angles that are more closely related to the orbital elements will provide a simpler control output. Therefore, the angles proven to give the simpler output from the study are used **[30]**.
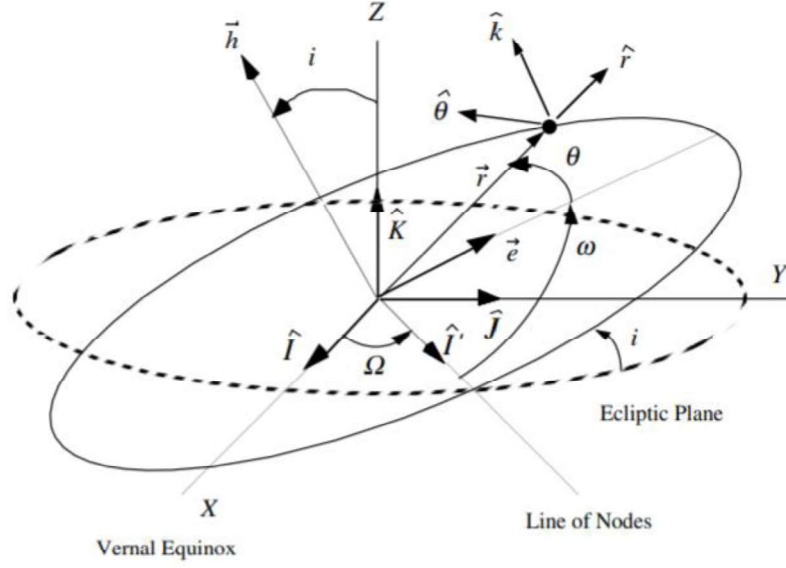
Figure 17: Orbital geometry used to define control angles [30]

Considering the coordinate frames presented in Figure 17, above, $\{\hat{I}, \hat{J}, \hat{K}\}$ represents the fixed, geocentric coordinate frame and $\{\hat{r}, \hat{\theta}, \hat{k}\}$ represents the orbital frame, where $\hat{r}$ is in the direction of $\vec{r}$, $\hat{\theta}$ is tangent to the orbit in the direction of the motion of the spacecraft, and $\hat{k}$ is the perpendicular vector outside of the orbital plane.

Using the $\{\hat{r}, \hat{\theta}, \hat{k}\}$ coordinate frame, the cone and clock angles, α and δ, are defined to transform the orbital frame to the body frame, as shown in Figure 18.
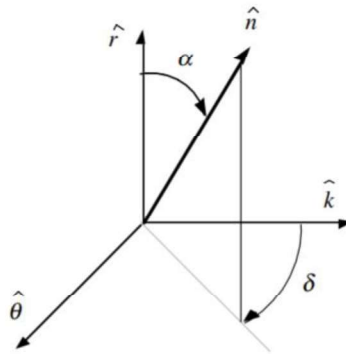
Figure 18: cone (α) and clock (δ) angles of the solar sail [30]

Therefore, to transform from the global frame, $\{\hat{I}, \hat{J}, \hat{K}\}$, to the body frame, $\{\hat{1}, \hat{2}, \hat{3}\}$, the orbital

elements must first be defined as quaternions using equations 3.3a-3.3e:

$$q_\alpha = \begin{bmatrix} \cos\left(\frac{\alpha}{2}\right) \\ 0 \\ \sin\left(\frac{\alpha}{2}\right) \\ 0 \end{bmatrix} q_\delta = \begin{bmatrix} \cos\left(\frac{\delta}{2}\right) \\ \sin\left(\frac{\delta}{2}\right) \\ 0 \\ 0 \end{bmatrix} q_{\theta+\omega} = \begin{bmatrix} \cos(\theta + \omega) \\ 0 \\ 0 \\ \sin(\theta + \omega) \end{bmatrix} q_i = \begin{bmatrix} \cos\left(\frac{i}{2}\right) \\ \sin\left(\frac{i}{2}\right) \\ 0 \\ 0 \end{bmatrix} q_\Omega = \begin{bmatrix} \cos\left(\frac{\Omega}{2}\right) \\ 0 \\ 0 \\ \sin\left(\frac{\Omega}{2}\right) \end{bmatrix} \quad (3.3a - 3.3e)$$

Assuming the vector, $\vec{v}$, is in the global $\{\hat{I}, \hat{J}, \hat{K}\}$ frame, it can then be transformed to the body

frame by defining the quaternion q_{trans} with equation 3.4 and 3.5.

$$q_{trans} = q_\alpha q_\delta q_{\theta+\omega} q_i q_\Omega \tag{3.4}$$

$$\vec{v}_{body} = q_{trans} \vec{v} q_{trans}^* \tag{3.5}$$

Where q_{trans}^* is the conjugate of q_{trans}.

Using q as the inertial attitude quaternion, the kinematic differential equations in terms of the

attitude quaternion is given in equation 3.6

$$\dot{q} = \frac{1}{2}\omega q \tag{3.6}$$

Where $q = \begin{bmatrix} q_1 \\ q_2 \\ q_3 \\ q_4 \end{bmatrix}$ with the real part of the quaternion defined as q_1.

The desired attitude quaternion from the commanded cone/clock angles, q_c, is equal to the

multiplication of q_{trans} with q_{trans}^*, as defined above. From this, the error is calculated using

equation 3.7.

$$e = qq_c^* \tag{3.7}$$

Where q_c^* is the conjugate of q_c.

The model of solar radiation pressure is taken from Bong Wie as well and shown in

equations 3.8 and 3.9 [30]. The force from the sun is assumed to come from the $\hat{J}$ direction.

$$\overrightarrow{F_{SRP}} = F_0(\hat{J} \cdot \hat{n})^2 \hat{n} \tag{3.8}$$

$$F_0 = \left(\frac{r_0}{r}\right)^2 a_c \tag{3.9}$$

Where r_0 = 1 Astronomical Unit (AU) and r is the magnitude of the r vector. a_c is the characteristic acceleration of the sail at 1 AU and is calculated using equation 3.10.

$$a_c = \frac{\eta P A}{m} \tag{3.10}$$

Where $P = 4.563 * 10^{-6} \frac{N}{m^2}$ is the nominal solar-radiation-pressure constant at 1 AU from the sun and η is the overall sail thrust coefficient, typically around 1.8 [29]. This will give the solar radiation pressure force of the sail in $\{\hat{I}, \hat{J}, \widehat{K}\}$, therefore the equation $\vec{v}_{body} = q_{trans}\vec{v}q_{trans}^*$ must be used to rotate it to the body frame. Once it is in the body frame, it is multiped by the distance between the spacecraft's cm/cp point to the sail to get τ_{SRP}.

c.) Orbital Dynamics

The orbital elements are needed to transform between the global $\{\hat{I}, \hat{J}, \widehat{K}\}$ frame and the fixed $\{\hat{1}, \hat{2}, \hat{3}\}$ body frame for calculating the solar radiation pressure. They are also needed to employ the steering laws applied to the cone and clock angles α and δ for orbit raising. The equations described in this section are explained in detail by Howard D. Curtis and Bong Wie [29] [31]. Initial X, Y, and Z coordinates are defined based on the initial launch condition of the satellite. The r vector is defined as $\vec{r} = X\hat{\imath} + Y\hat{\jmath} + Z\hat{k}$. r is then calculated from equation 3.11.

$$r = \sqrt{\vec{r} \cdot \vec{r}} = \sqrt{X^2 + Y^2 + Z^2} \tag{3.11}$$

Initial velocity is also calculated based on approximate launch conditions. The v vector is defined as $\vec{v} = V_x\hat{\imath} + V_y\hat{\jmath} + V_z\hat{k}$. v is then calculated from equation 3.12.

$$v = \sqrt{\vec{v} \cdot \vec{v}} = \sqrt{V_x{}^2 + V_y{}^2 + V_z{}^2} \tag{3.12}$$

The specific angular momentum vector and magnitude is calculated from equations 3.13 and 3.14.

$$\vec{h} = \vec{r} \times \vec{v} \tag{3.13}$$

$$h = \sqrt{\vec{h} \cdot \vec{h}} \tag{3.14}$$

The lines of nodes if calculated from equation 3.15.

$$\vec{N} = \hat{k} \times \frac{\vec{h}}{h} \tag{3.15}$$

The longitude of the ascension node, Ω can be defined using equation 3.16.

$$\Omega = cos^{-1}\left(\frac{n_k}{|\vec{N}|}\right) \tag{3.16}$$

Where n_k is the $\hat{k}$ component of the line of nodes vector. The inclination can also be calculated from the angular velocity using equation 3.17.

$$i = cos^{-1}\left(\hat{k} \cdot \frac{\vec{h}}{h}\right) \tag{3.17}$$

The eccentricity can be obtained from Earth's gravitational constant, µ, from equation 3.18

$$e = \frac{1}{\mu}\left(|\vec{V}|^2 - \frac{\mu}{r}\right)\vec{r} - rV_r\vec{V} \tag{3.18}$$

Where V_r is the velocity in the radial direction defined as $V_r = \frac{\vec{r} \cdot \vec{V}}{|\vec{r}|}$. Then, the true anomaly, θ is calculated from equation 3.19.

$$\theta = \begin{cases} cos^{-1}\left(\frac{\vec{e}}{e} \cdot \frac{\vec{r}}{r}\right) & if \ v_r \geq 0 \\ 360 - cos^{-1}\left(\frac{\vec{e}}{e} \cdot \frac{\vec{r}}{r}\right) & if \ v_r < 0 \end{cases} \tag{3.19}$$

The eccentricity is also related to the argument of periapsis, ω, according to equation 3.20

$$\omega = \begin{cases} \cos^{-1}\left(\vec{N} \cdot \dfrac{\vec{e}}{|\vec{e}|}\right) & if\ e_k \geq 0 \\ 360 - \cos^{-1}\left(\vec{N} \cdot \dfrac{\vec{e}}{|\vec{e}|}\right) & if\ e_k < 0 \end{cases} \tag{3.20}$$

Where e_k represents the $\hat{k}$ component of the eccentricity vector. To ensure orbit raising, α and δ

are defined using equations 3.21 and 3.22

$$\alpha = \begin{cases} \pi & if\ \sin(\theta + \omega) \leq 0 \\ \dfrac{\pi}{2} & if\ \sin(\theta + \omega) > 0 \end{cases} \tag{3.21}$$

$$\delta = 0 \tag{3.22}$$

After these orbital elements are calculated, $\vec{r}$ and $\vec{v}$ can then be updated by integrating equation

3.23.

$$\ddot{\vec{r}} + \frac{\mu}{r^3}\vec{r} = \vec{F}_{SRP} \tag{3.23}$$

d.) Controller Derivation

Both the PID and SMC can now be derived.

PID

The PID controller will simply be defined as

$$u = sat\left(K_p error + K_i \int (error * dt) + K_d \dot{error}\right) \tag{3.24}$$

Where K_p, K_i, and K_d are the proportion, integral, and derivative controller gains, respectively. q

is the attitude quaternion and $error$ is the error calculated between the control quaternion and

the attitude quaternion is shown in equation 3.7. Since the output will be a quaternion, only the

vector portion of the control will be used and applied to the attitude dynamics based on its

corresponding components. To account for real-world actuator constraints, a saturation function

is used on the control, imposing a maximum torque value. This is done using the logic presented in equation 3.25

$$sat(x) = \begin{cases} x & if\ |x| < u_{max} \\ u_{max} * sign(x) & otherwise \end{cases} \qquad (3.25)$$

Where u_{max} is the maximum amount of torque produced by the reaction wheel. The K_p, K_i, and K_d are first tuned using Zeigler-Nichols method and are then manually tuned to improve settling time. The steps used for the Ziegler-Nichols method are shown in the results section. To make tuning more manageable, the gains are tuned to 2 significant figures.

SMC

The sliding mode controller begins by re-defining ω such that it will drive the system to the sliding surface, defined in equation 3.26.

$$\omega = -\lambda \ln(error) \qquad (3.26)$$

Where λ is a tuning parameter that defines how quickly the system will approach the sliding surface and $error$ is the error quaternion defined in the attitude dynamics and kinematics section above. Recall the unit quaternion definition, $q = \cos(\theta) + \vec{u}\sin(\theta)$, where $\vec{u}$ is the vector component of the quaternion and θ defines the angle of rotation about the Euler axis. Use Euler's identity for complex numbers to define $q = e^{\vec{u}\theta}$. Now the logarithm of the error quaternion can be derived as $\vec{u}\theta$. By setting the sliding surface to $-\lambda|\vec{u}\theta|$, it can be seen that the error quaternion will always be driven towards zero [32]. While other functions may be used for the sliding surface, the natural logarithm function is used because it guarantees local asymptotic stability, as proven in the next section, unlike a quadratic function, which cannot always guarantee local asymptotic stability. Once the sliding surface is reached, it will guide the system to the equilibrium point at a faster rate using a logarithmic function over a linear function. λ is also tuned manually until the lowest settling time is reached.

Now, define a function that calculates the distance between the current state of the system and the sliding surface. In this case, it was defined using equation 3.27.

$$\sigma = \omega - \lambda \log(error) \tag{3.27}$$

This function will drive the system to the sliding mode, and once it gets there, it will switch back and forth on the sliding mode, forcing it to equilibrium. The control can finally be defined using equation 3.28.

$$u = -u_{max} sign(\sigma) \tag{3.28}$$

To mathematically show the limitations of the sliding mode controller, consider the derivative of the sigma function shown in equation 3.29.

$$\dot{\sigma} = \dot{\omega} - \lambda \dot{error} * error^* = \frac{\omega \times J\omega + \tau_{SRP} - u_{max} sign(\sigma)}{J} - \lambda \dot{error} * error^* \tag{3.29}$$

Since the desire is to drive σ to zero, $\dot{\sigma} \leq 0$. Therefore, $u_{max} > -J * \lambda * \dot{error} * error^* + \omega \times J\omega + \tau_{SRP}$. If this condition is not met, then u_{max} will not be sufficient to control the system.

Stability Proof

To prove Lyapunov stability for the sliding surface, first derive the Lyapunov function using equation 3.30.

$$V = \frac{1}{2}\log(error)^2 \tag{3.30}$$

Taking the derivative of this results in equation 3.31

$$\dot{V} = \log(error)\frac{1}{error}\dot{error} \tag{3.31}$$

After differentiating the *error* quaternion, the derivative of the Lyapunov function is shown in equation 3.32.

$$\dot{V} = \frac{1}{2}log(error)\omega = -\frac{1}{2}\lambda log(error)^2 = -\lambda V \tag{3.32}$$

Since V is greater than 0 for all states not equal to the equilibrium point, $\dot{V}$ is proven to be ≤ 0 for all states not equal to the equilibrium point, and $\dot{V}$ is not identically 0 for any state other than the equilibrium point, local asymptotic stability is proven using Lyapunov's second stability theorem [29]. It is important to note that since $error$ is a unit quaternion, it is confined by a unit sphere in 4-D space, allowing the stability proof to hold true for all values of $error$.

Chapter IV:

Results and Discussion

Orbital Dynamics Verification

The orbital dynamics can be verified using conservation of energy. The orbital energy should remain constant throughout the entirety of the orbit. The energy of the orbit was calculated using $E = \dfrac{v^2}{2} - \dfrac{\mu}{r}$

Table 2: Relationship between the time step and change in orbital energy

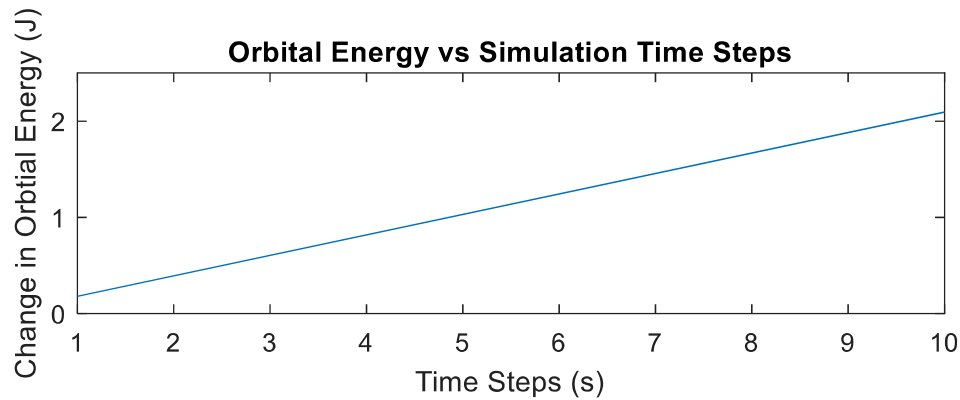| Time Step (s)	ΔEnergy (J)	Percent Error
0.01	0.0018	0.007%
0.1	0.0178	0.073%
1	0.1805	0.74%
10	2.0934	8.6%

Figure 21: Linear relationship between the change in orbital energy and the time step of the simulation

The change in orbital energy throughout the orbit is shown in Table 2. Due to computer rounding, the difference in orbital energy calculated is directly related to the time step of the simulation. The graph in Figure 21 shows the change in orbital energy as a function of the time

step value of the simulation. As shown, as the time step decreases, the change in orbital energy also decreases. This trend implies that with an infinitely small timestep, the change orbital energy will converge to be zero. Since the maximum orbital energy is 24.39 J, when the time step is set above 0.5, the simulation becomes unstable due to the finite number of significant figures imposed by computer hardware. Therefore, the time step chosen for this thesis is 0.1 due to the more reliable numerical stability and runtime of the simulation.

Response to Varying Maximum Torque

a.) PID

The PID controller was tuned manually for each new u_{max} value. The state response with no control input is shown in Figure 22, where q1 represents the scalar term of the quaternion and q2, q3, and q4 represent the roll, pitch, and yaw axis, respectively.
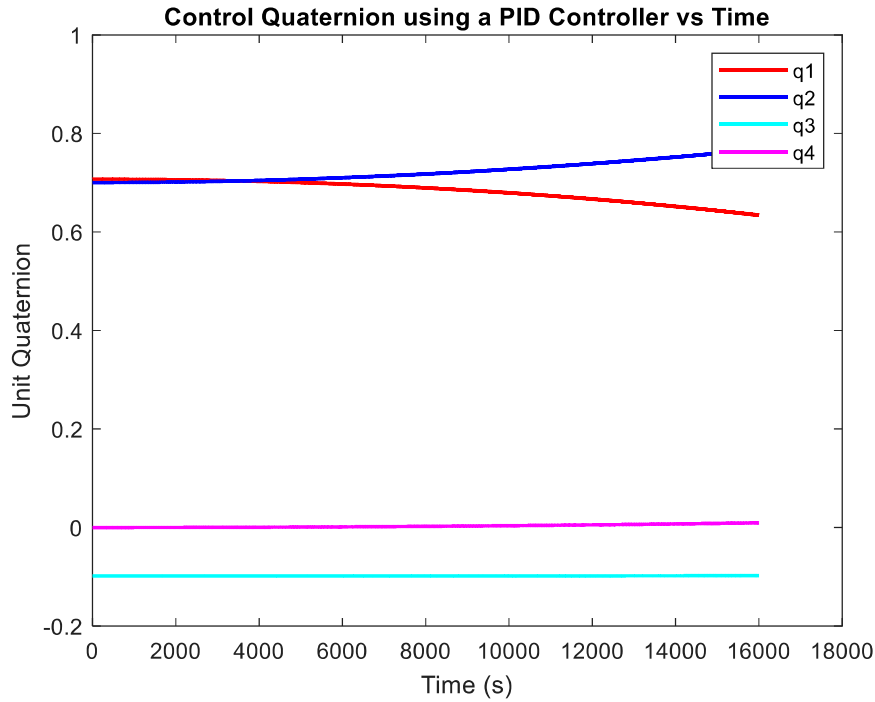
Figure 22: State response with no control input

The gains of the PID controller were first approximated using the Zeigler-Nichols tuning method. The K_i and K_d gains are first set to zero and the K_p gain is increased from zero until the output reaches a steady oscillation. This value is denoted as K_{cr} the period of the oscillation is denoted T_{cr}. The initial guess of the PID gain values can now be found from equations 4.1a-4.1c [33].

$$K_p = 0.6K_{cr} \tag{4.1a}$$

$$K_i = \frac{1.2K_{cr}}{T_{cr}} \tag{4.1b}$$

$$K_d = \frac{3K_{cr}T_{cr}}{40} \tag{4.1c}$$

Using $u_{max} = 10mNm$, the response of the system when $K_p = K_{cr}$ is shown in Figure 23.
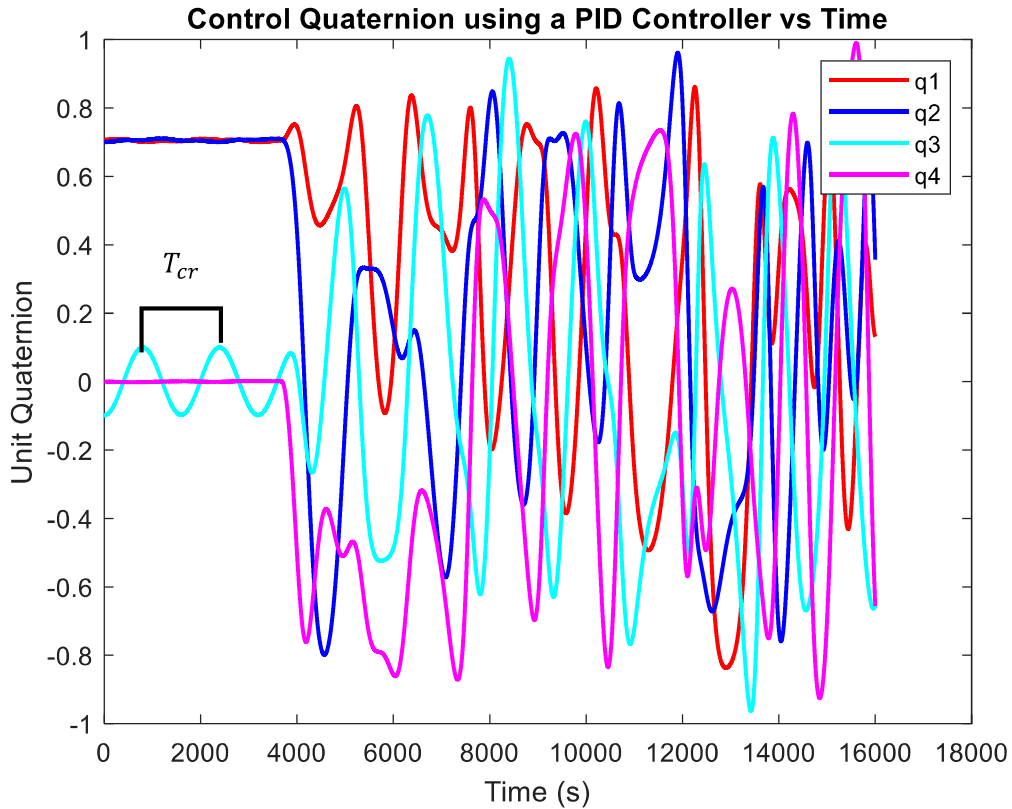
Figure 23: Steady oscillation used to find T_{cr} when $K_{cr} = 1$

In this case, K_{cr} is found to be 1 and T_{cr} is 1,610s. Therefore, K_p=0.6, $K_i = 7.5 * 10^{-4}$, and $K_d = 120$. The system response using these gains is shown in Figure 24.
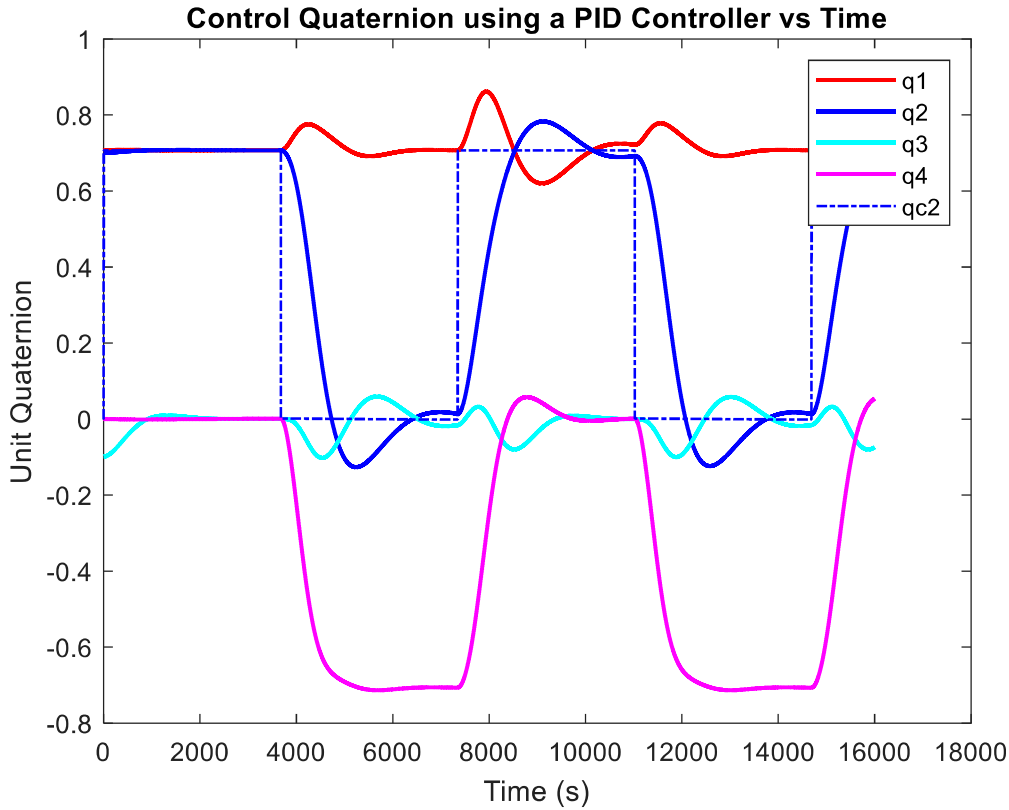
Figure 24: System response using a PID controller with gains tuned using Ziegler-Nichols method with the desired control q_{c2}

While this is a good starting point, the goal is to achieve the lowest settling time and state response error. Settling time is calculated by subtracting the time at which the roll axis first reaches zero by the time the roll axis from the controller is within 2% of zero. State response error is calculated by taking the difference between the actual attitude quaternion and the desired attitude quaternion for each time step, finding the sum, and normalizing over the simulation runtime. By keeping the time step and runtime of the simulation the same for every run, the state response error can be reasonably compared. K_d controls how fast the rate of the error is driven to zero. Therefore increasing K_d will have a more significant effect on reducing the settling time. It was found that increasing K_d to 190 provides a response that improves the settling time of the

roll axis while overshoot to stay within 2% of the desired response. K_p is more closely related to state response error since it controls error directly. After tuning the K_d gain, it was found that slightly reducing K_p to 0.59 also improved the settling time, resulting in the time shown in Table 3. Increasing K_i also increased the settling time while decreasing K_i did not change the settling time. Therefore, K_i was kept the same. To make tuning the PID controllers more manageable, the

Figure 25: State response using a PID controller with gains K_p=0.59, K_i = $7.5 * 10^{-4}$, and $K_d = 190$ for u_{max} = 10 mNm with the desired control q_{c2}

gains are tuned to a maximum of 2 significant figures. A plot of the response is shown in Figure 25. These steps were repeated for different u_{max} values. Table 3 shows the initial Zeigler-Nichols coefficients, the manually tuned coefficients and each set of coefficients respective settling times and state response error calculated from q_2.

Table 3: Corresponding controller gains, settling times, and state response errors

PID Controller

u_{max} [mNm]	Tuning Method	K_p	K_i	K_d	Settling time (q_2)	State response error (q_2) [radians/s]
10	Ziegler-Nichols	0.60	$7.5 * 10^{-4}$	120	2520s	12.6
10	Manual	0.59	$7.5 * 10^{-4}$	190	1580s	13.4
0.5	Ziegler-Nichols	12	0.014	2700	3600s	21.8
0.5	Manual	7.1	0.014	2900	2340s	21.1
0.2	Ziegler-Nichols	6.0	0.0034	2600	Does not settle	35.9
0.2	Manual	4.9	0.0034	3300	3590s	35.8

Sliding mode Controller

u_{max} [mNm]	Tuning Method	λ	Settling time [s]	State Response error (q_2) [radians/s]
10	Manual	0.015	481s	4.48
0.5	Manual	0.00359	1900s	19.5
0.2	Manual	0.0023	2960s	31.3

Since the goal is to test low maximum torque values, the next maximum torque value analyzed is 0.5 mNm. The state response for this u_{max} value after the manual tuning is shown in Figure 26.

As shown in table 3, the settling time increases by 790s when u_{max} is increased from 10 mNm to 0.5mNm, even when using PID gains tuned to minimize the settling time. When applying $u_{max} = 0.1$ mNm, the state response error of q_2 increases significantly from 13.4 rad/s to 35.8 rad/s, shown in Figure 27. With the PID gains tuned to maximum settling time about the roll axis (corresponding to q2 on the figure), the system response does not remain stable around the desired response for very long.
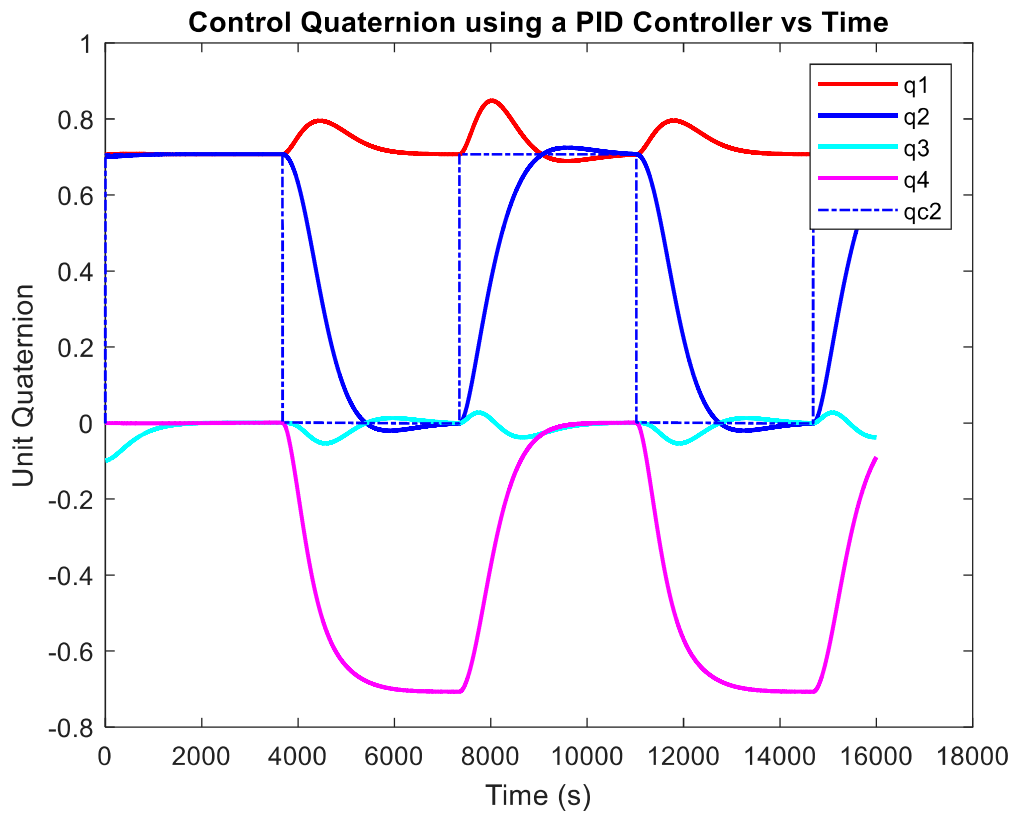
Figure 26: State response using a PID controller with gains K_p=0.71, $K_i = 0.014$, and $K_d = 2900$ for u_{max} = 0.5 mNm with the desired control q_{c2}

Figure 27: State response using a PID controller with gains K_p=4.9, $K_i = 0.0034$, and $K_d = 3300$ for u_{max} = 0.2 mNm with the desired control q_{c2}

b.) SMC

Since the sliding mode controller only has one controller gain, tuning is simpler compared to

the PID controller. The controller gain, λ, is related to how fast the system converges to the

sliding surface. Setting λ too low, in this case 0.003, will increase the settling time, as shown in

Figure 28.
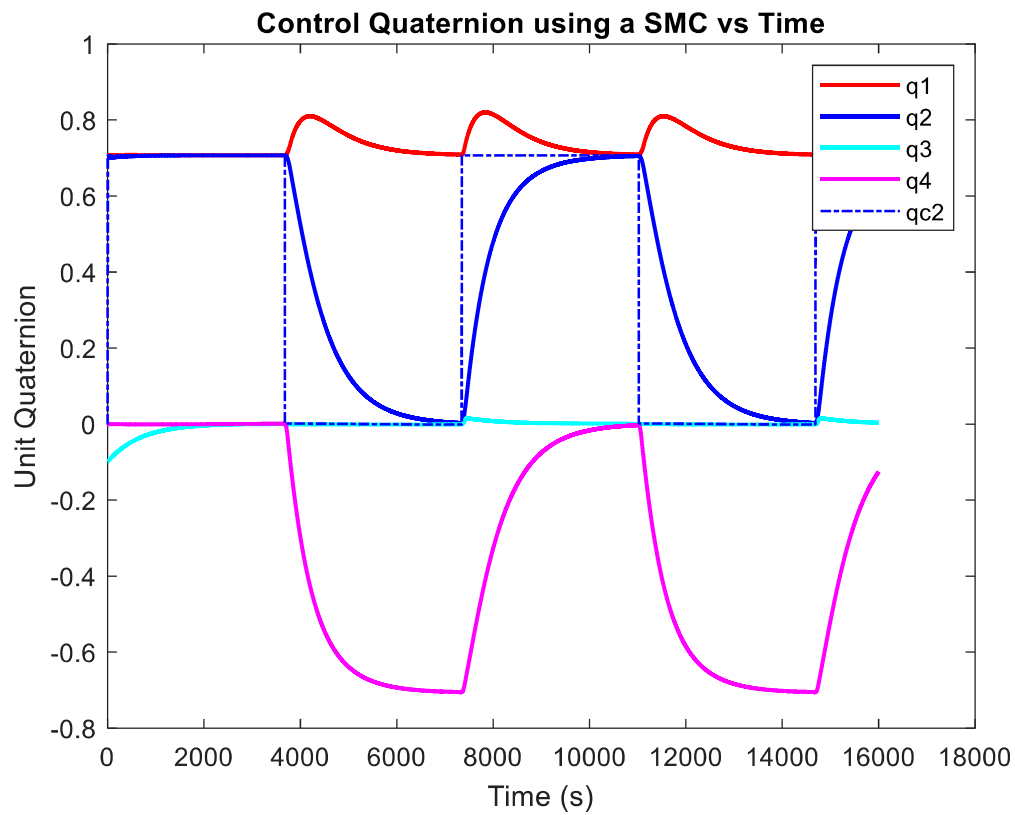

Figure 28: State response using a sliding mode controller where $\lambda=0.003$ and $u_{max}=10mNm$

However, setting λ too high, in this case 0.1, will cause overshoot, resulting in unwanted
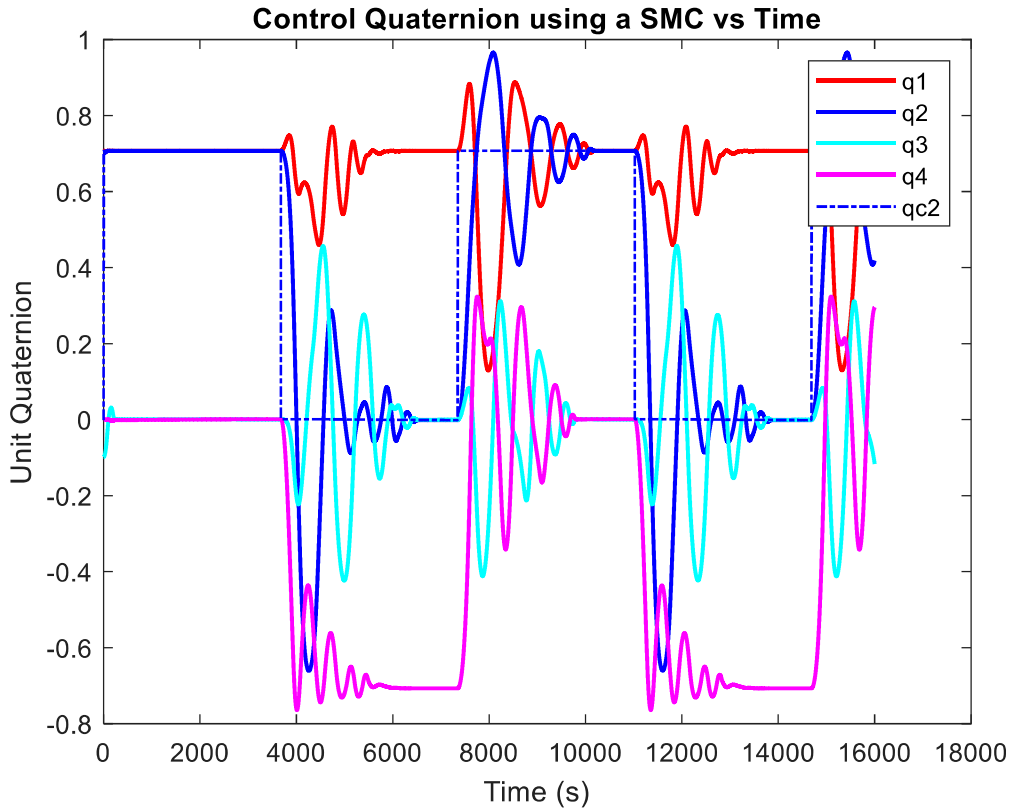
oscillations, as shown in Figure 29.

Figure 29: State response using a sliding mode controller where λ=0.1 and u_{max}=10mNm

Therefore, λ is chosen based on which value produces the shortest settling time. From manual

tuning, it was found λ=0.015 produces a state response with the shortest settling time when

u_{max}=10mNm. The state response is shown in Figure 30.

Table 3 shows that the sliding mode controller has a shorter settling time than the PID

controller that was also tuned for minimum settling time at the same u_{max} value. The state

response using a SMC for u_{max} values equal to 0.5 mNm and 0.2 mNm is shown in Figures 31

and 32. It is also shown in Table 3 that the settling time for the sliding mode controller is

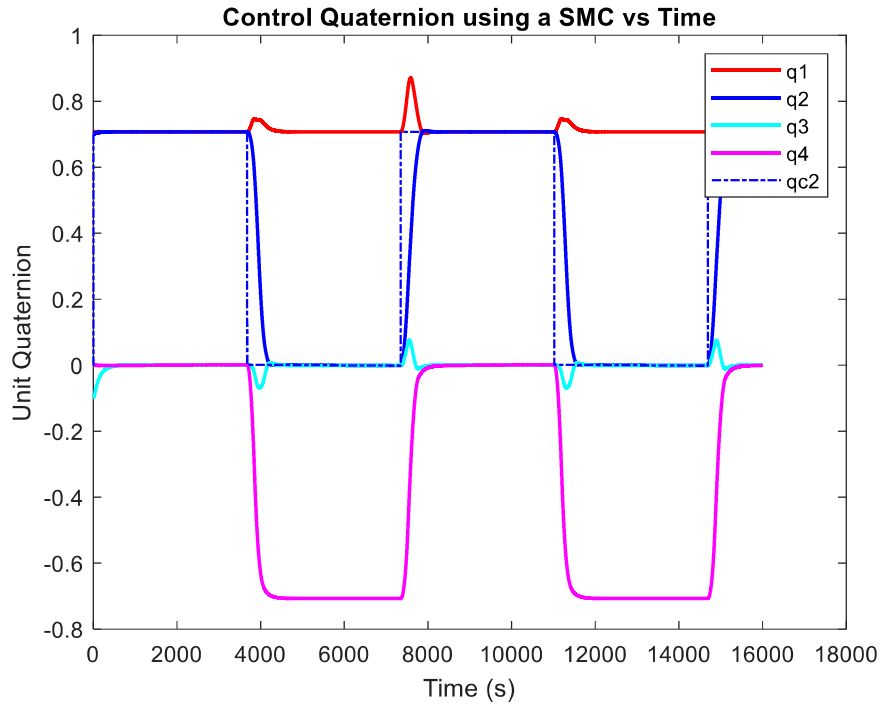consistently shorter for different maximum torque values.

Figure 30: State response using a sliding mode controller where λ=0.015 and u_{max}=10mNm
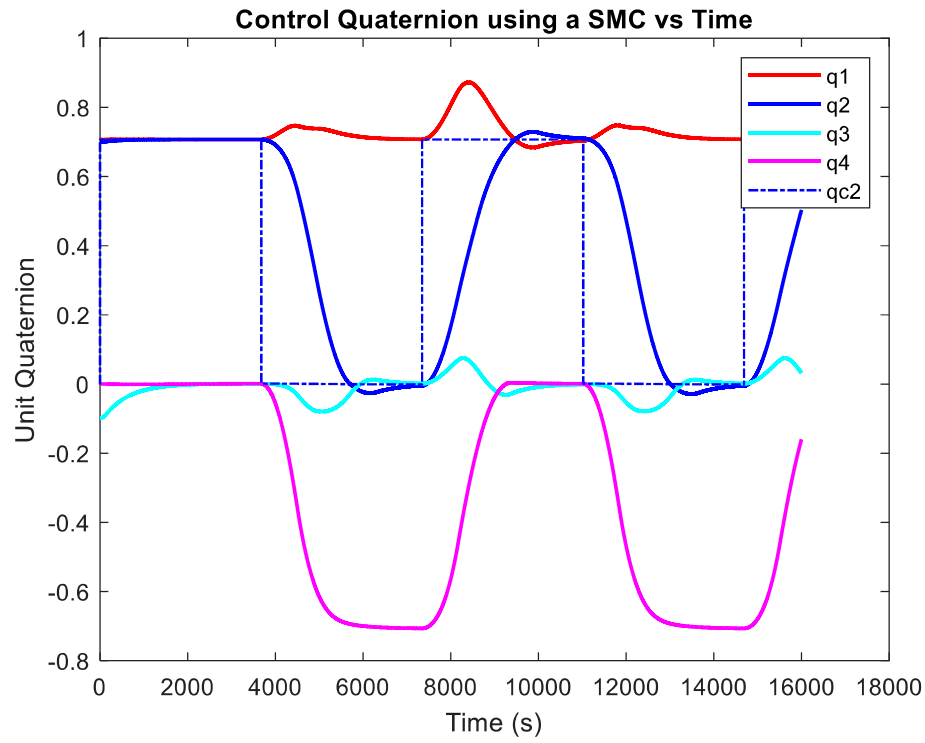
Figure 31: State response using a sliding mode controller where λ=0.00359 and u_{max}=0.5mNm
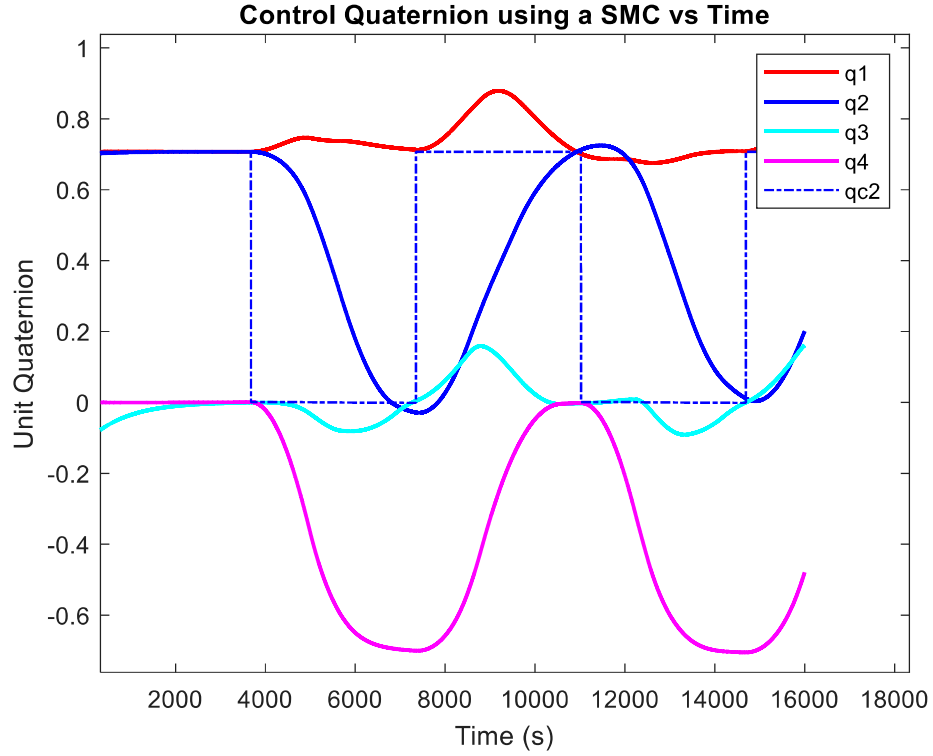
Figure 32: State response using a sliding mode controller where λ=0.0023 and
u_{max}=0.2mNm

Performance Analysis with Constant Maximum Torque

Since the smallest maximum torque value is the most prone to reaction wheel saturation

causing instability, that is the constant maximum torque value chosen to effectively compare the

performance of the SMC and the PID controller. As shown in Table 3, the SMC has a shorter

settling time than the PID controller. However, state response error should also be analyzed in

this case since a lower state response error about the roll axis corresponds to more efficient

production of thrust. The state response error for the SMC and PID controller about the roll axis

is shown in Figure 33.
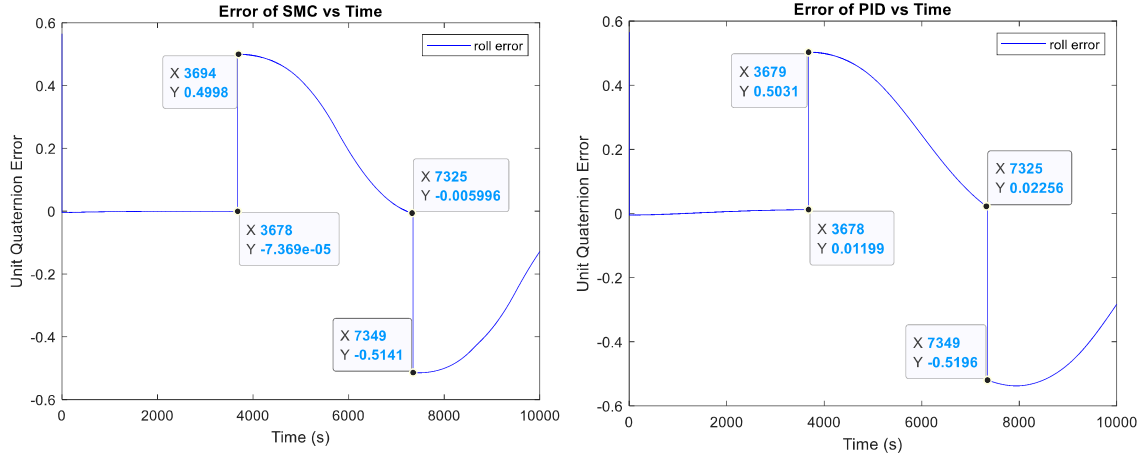
Figure 33: Error about the roll axis for a PID controller (right) and a SMC (left)

While these results are very similar, Table 3 shows the sum of the state response error of the

SMC is 4.5 rad/s less than the PID controller.

Another important output to analyze is the controller output torque. Since a SMC already

switches from minimum to maximum output torque values, the time at which a control torque is

sustained before it switches to the next maneuver is the time being considered. Comparing the
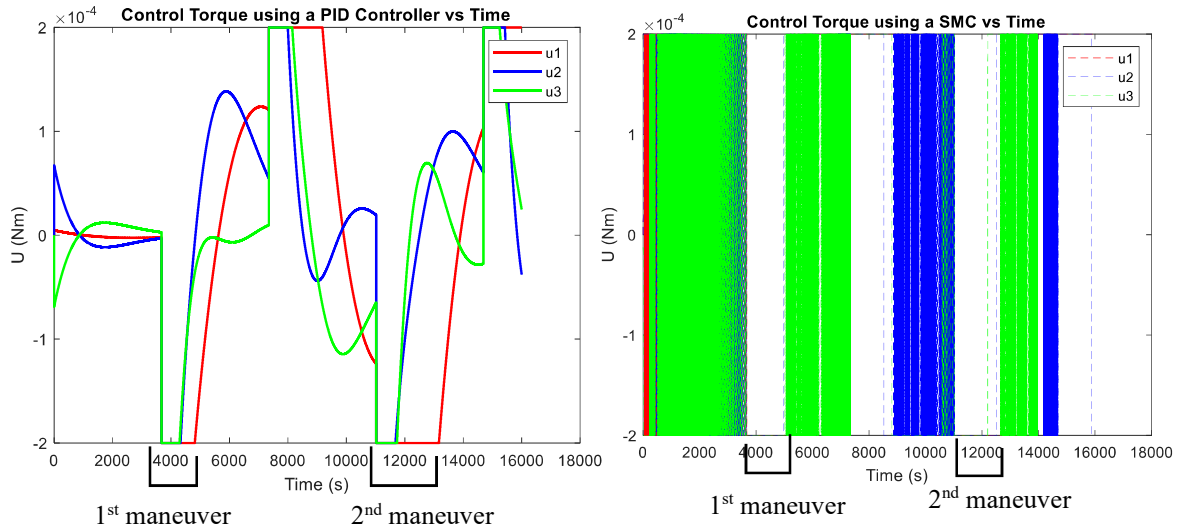
Figure 34: Control torque output for PID controller (left) and SMC (right)

output torques from the two controllers in Figure 34 and Table 4 shows that the PID controller is

at maximum significantly less than the sliding mode. The main reason for this is because the

sliding mode controller is restricted to either maximum or minimum while the PID controller can be any value in between. Therefore, using this method to compare the PID controller to the sliding mode is not a fair comparison.

Table 4: Comparison of time spent at maximum control torque

|		Time at max after 1ˢᵗ maneuver [s]	Time at max after 2ⁿᵈ maneuver [s]	Total time at max [s]
SMC	U_1	2009	3744	5753
	U_2	1313	1830	3143
	U_3	1334	2943	4277
			Sum of total time:	***13,173***
PID	U_1	1135	2150	3285
	U_2	646	660	1306
	U_3	614	710	1324
			Sum of total time:	***5915***

A fairer comparison would be to replace the sign function in the sliding mode controller to the saturation function used on the PID controller. This way, the sliding mode controller has the same output restrictions as the PID controller. The state response and output control torque using a saturation function for the SMC is shown in Figure 35. Using this method eliminates reaction wheel saturation, but significantly increases the state response error. This suggests that reaction wheel saturation may be necessary to produce a stable response when using smaller reaction wheels. Therefore, the amount of time a reaction wheel is saturated should be a secondary concern compared to settling time and state response error.

However, one metric that is related to the amount of time a reaction wheel is saturated that may be a higher concern is the actuation energy. This is characterized by the area under the torque curve. Table 5 compares the PID controller to the SMC when the sign function is used and when the sigmoid function is used.

As expected, the SMC with the sign function showed to have the highest amount of actuation energy. The SMC with the saturation function showed to have the lowest, but at a

major cost to performance compared to both the SMC with the sign function and the PID

controller. Therefore, in terms of actuation energy, the PID controller is the best choice to

balance performance and energy. However, modeling improvements may be made to the SMC

controller with the sign function that could reduce actuation energy. This will be discussed

further in the following section.

Table 5: Performance comparison of PID and two different sliding mode controllers

	PID	*SMC (sign)*	*SMC (sat)*
U_1 *[J]*	2.1201	1.933	0.9473
U_2 *[J]*	2.1796	3.0103	0.0180
U_3 *[J]*	0.6998	1.6751	0.0498
Sum [J]	*4.9995*	*6.6184*	*1.0151*
Settling Time [s]	*2590*	*3590*	*Does not settle*
State response error [rad/s]	*35.8*	*31.3*	*38.3*

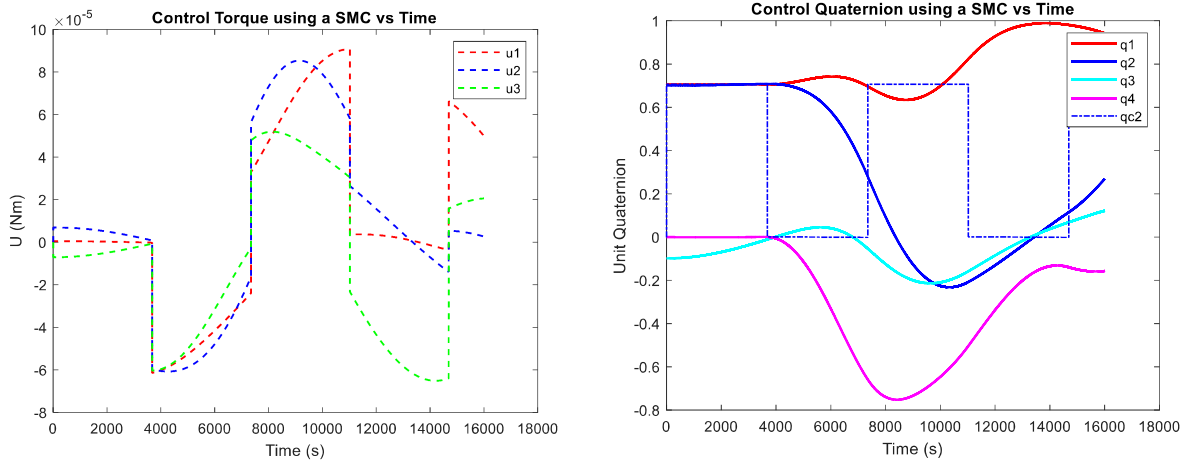*Figure 35: Control torque output (left) and system response (right) of a sliding mode controller using a saturation function with λ=0.394 and u_{max}=0.2mNm*

Chapter V:

Conclusion

In this thesis, the settling time and system response were analyzed for a PID and a sliding mode controller for a range of maximum control torque values. Then, for a constant maximum torque value, the settling time, controller output torque, actuation energy, and state response error of the roll angle were analyzed. The data presented in this thesis shows that the SMC has improved performance, compared to a PID controller, in terms of settling time and stability when tested over a range of maximum torque values. A summary of the performance difference is given in Table 6.

Table 6: Difference between SMC and PID controller in terms of settling time and state response error

u_{max} [mNm]	*Percent Improvement in Settling time [s]*	*Percent Improvement in State Response Error (q_2)*	*Best Performing Controller*
10	69.5%	66.6%	SMC
0.5	18.8%	7.7%	SMC
0.2	14.4%	17.5%	SMC

The PID controller showed to produce reaction wheel saturation for a shorter period than a SMC with a sign function. However, when a saturation function was employed with the SMC, it was shown to produce no reaction wheel saturation but with a cost of reduced controller performance. This suggests two things. One being that reaction wheel saturation may be necessary for producing a stable state response with a short settling time and small state response error. The other being that even small modifications to the SMC can produce very different results and more research must be done on its potential to limit reaction wheel saturation while still producing a favorable state response. Because the SMC employing a sign function showed

to produce more reaction wheel saturation, it also results in a higher actuation energy than the PID controller.

Based on the results presented in this thesis, the sliding mode controller is advantageous over the PID controller in terms of state response performance and settling time, especially in cases with higher maximum torques. However, if power draw is a significant concern, a PID controller may be a better solution, or modifications to the sliding mode controller should be researched.

Future Work

The actuation energy may be improved by including an electromechanical model of the reaction wheel and defining the sliding mode controller to control voltage rather than torque. The discontinuous behavior of the SMC employing a sigmoid function relates more closely to switching voltage than switching torque, since there is a more significant time delay when switching torque.

The addition of a sliding mode observer has been shown to improve robustness of the controller and may also aid in robustness under actuator limitations [34]. A sliding mode observer improves performance in real-world implementation due to its ability to filter and weigh sensor data.

Deriving a sliding mode controller via backstepping method has been shown to improve reaction wheel saturation [35]. The use of recursive Lyapunov functions allows for the controller to compensate or nonlinear disturbances and take advantage of stabilizing nonlinearities simultaneously.

References

[1] J. Verne, From the Earth to the Moon, 1856.

[2] A. A. Siddiqi, Beyond Earth A Chronicle of Deep Space Exploration, 1958-2016, Washington, DC: NASA History Program Office, 2018, pp. 121-122.

[3] "MESSENGER Sails on Sun's Fire for Second Flyby of Mercury," 2008.

[4] "MTSAT," n.d.. [Online]. Available: https://earth.esa.int/web/eoportal/satellite-missions/m/mtsat#foot7%29.

[5] J. Kawaguchi, T. Kominato and K. Shirakawa, "Attitude Control Flight Experience: Coping with Solar Radiation and Ion Engines Leak Thrust in Hayabusa (MUSES-C)," in *20th ISSFD Conference*, Annapolis, 2007.

[6] Y. Tsuda, O. Mori, R. Funase, H. Sawada, T. Yamamoto, T. Saiki, T. Endo and J. Kawaguchi, "Flight status of IKAROS deep space solar sail demonstrator," *Acta Astronautica,* vol. 69, no. 9, pp. 833-840, 2011.

[7] "LightSail Flight by Light for CubeSats," [Online]. Available: https://www.planetary.org/explore/projects/lightsail-solar-sailing/.

[8] S. N. Adeli, "Attitude Control and Deployment of Nano-Solar Sail Spacecraft," University of Surrey, 2011.

[9] B. Wie, "Solar Sail Attitude Control and Dynamics, Part Two," *Journal of Guidance, Control, and Dynamics,* vol. 27, no. 4, pp. 536-544, 07 2004.

[10] R. J. McKay, M. Macdonald, J. Biggs and C. R. McInnes, "Survey of Highly Non-Keplerian Orbits with Low-Thrust Propulsion," *Journal of Guidance, Control, and Dynamics,* vol. 34, no. 3, pp. 645-666, 2011.

[11] "About Space Debris".*European Space Agency.*

[12] R. P. a. V. Schaus, "The Legal Framework for Space Debris Remediation as a Tool for Sustainability in Outer Space," *aerospace,* p. 11, 2018.

[13] C. Pardini and L. Anselmo, "Assessment of the consequences of the Fengyun-1C breakup in low Earth orbit," *Advances in Space Research,* vol. 44, no. 5, pp. 545-557, 2009.

[14] "Mitigating Space Debris".*European Space Agency.*

[15] D. King-Hele, "The Effect of the Earth's Oblateness on the Orbit of a Near Satellite," *Royal Society of London. Series A, Mathematical and Physical Sciences ,* vol. 247, no. 1248, pp. 49-72, 1958.

[16] S. Clark, "Collision between Rocket Stages Doomed Falcon 1," *SpaceFlight Now,* 2008.

[17] C. Katan and D. Lanning, "NASA's Next Solar Sail: Lessons from NanoSail - D2".

[18] E. Berger, "So How Much Did The Planetary Society's LighSail Really Sail?," 2019. [Online]. Available: https://arstechnica.com/science/2019/08/so-how-much-did-the-planetary-societys-light-sail-really-sail/.

[19] R. L. Burton, J. K. Laystrom-Woodard, G. F. Benavides, D. L. Carroll, V. L. Coverstone, G. R. Swenson, A. Pukniel, A. Ghosh and a. A. D. Moctezuma, "Inital Development of the CubeSail/UltraSail Spacecraft," 2010.

[20] A. Pukniel, V. Coverstone, R. Burton and D. Carroll, "The dynamics and control of the CubeSail mission: A solar sailing demonstration," *Advances in Space Research,* vol. 48, pp. 1902-1910, 2011.

[21] S. N. L. V. J. & W. B. Adeli, "A scalable bus-based attitude control system for Solar Sails," *Advances in Space Research,* vol. 48, no. 11, pp. 1836-18847, 2011.

[22] B. A. Plante, D. A. Spencer, B. Betts, S. Chait, J. M. Bellardo, A. Diaz and I. Pham, "LightSail 2 ADCS: From Simulation to Mission Readiness," 2016.

[23] J. Davis, "Here's What We've Learned So Far From LightSail 2," 10 January 2020. [Online]. Available: https://www.planetary.org/blogs/jason-davis/heres-what-we-learned-so-far-ls2.html.

[24] X. Lian, J. Liu, C. Wang and T. Yuan, "RBF network based adaptive sliding mode control for solar sails," *Aircraft Engineering and Aerospace Technology,* vol. 90, no. 8, pp. 1180-1191, 2018.

[25] Y. Chen, R. Qi, H. Wang and Z. Jiang, "Adaptive Second-order Sliding Mode Station-keeping Control for Solar Sail Spacecraft on Displaced Orbit," in *38th Chinese Control Conference*, Guangzhou, China, 2019.

[26] R. Funase, Y. Shirasawa, Y. Mimasu, O. Mori, Y. Tsuda, T. Saiki and J. Kawaguchi, "On-orbit verification of fuel-free attitude control system for spinning solar sail utilizing solar radiation pressure," *Advances in Space Research,* vol. 48, pp. 1740-1746, 2011.

[27] "RW210," Hyperion Technologies B.V., 2019.

[28] "RW400," Hyperion Technologies, 2019.

[29] B. Wie, Space Vehicle Dynamics and Control, 2nd ed., Reston, VA: American Institute of Aeronautics and Astronautics, Inc., 2008.

[30] B. Wie, "Thrust Vector Control Analysis and Design," *Journal of Spacecraft and Rockets,* vol. 44, no. 3, pp. 545-557, 2007.

[31] H. D. Curtis, Orbital Dynamics for Engineering Students, 3rd ed., Elsevier, 2014.

[32] A. A. Wijaya, Wahyudi, R. Akmeliawati and F. J. Darsivan, "Natural logarithm sliding mode control (ln-SMC) using EMRAN for active engine mounting system,," in *2010 11th International Conference on Control Automation Robotics & Vision*, Singapore, 2010.

[33] J. Ziegler and N. Nichols, "Optimum Settings for Automatic Controllers," *Transactions of the ASME,* vol. 64, pp. 759-768, 1942.

[34] B. Xiao, Q. Hu and Y. Zhang, "Adaptive Sliding Mode Fault Tolerant Attitude Tracking Control for Flexible," *IEEE TRANSACTIONS ON CONTROL SYSTEMS TECHNOLOGY,* vol. 20, no. 6, pp. 1605-1612, 2012.

[35] B. Xaio, Q.-L. Hu and G. Ma, "Adaptive sliding mode backstepping control for attitude tracking of flexible spacecraft under input saturation and singularity," *Journal of Aerospace Engineering,* vol. 224, no. G2, pp. 199-214, 2010.

[36] B. Wie, "Solar Sail Attitude Control and Dynamics Part 1," *Journal of Guidance, Control, and Dynamics,* vol. 27, no. 4, pp. 526-535, 07 2004.

[37] J. Orphee, B. Diedrich, B. Stilltner, C. Becker and A. Heaton, "Solar sail attitude control system for the NASA Near Earth Asteroid Scout Mission.," 2017.

[38] S. Firuzi and S. Gong, "Attitude Control of a Flexible Solar Sail in Low Earth Orbit," *Journal of Guideance, Control, and Dynamics,* vol. 41, no. 8, pp. 1715-1730, 2018.

[39] J. Baculi and M. A. Ayoubi, "FUZZY ATTITUDE CONTROL OF SOLAR SAIL WITH TRANSLATING CONTROL MASSES VIA LINEAR MATRIX INEQUALITIES," in *26th AAS/AIAA Space Flight Mechanics Meeting*, 2016.

[40] "The Evolution of Sail and Sailing Through the Ages," *Amerian Sailing Association,* 15 November 2017.

[41] G. Greschik, B. Derbes, G. Veal and J. Rogan, "The Cord Mat Sail - Concept, Mechanics, and Design Example," in *46th AIAA/ASME/ASCE/AHS/ASC Structures, Structural Dynamics and Materials Conference*, Austin, TX, 2005.

[42] D. C. Ullrey, S. Soleymani, A. Heaton, J. Orphee, L. Johnson, R. Sood, P. Kung and S. M. Kim, "Strong Solar Radiation Forces from Anomalously Reflecting Metasurfaces for Solar Sail Attitude Control," *Scientific Reports,* vol. 8, no. 1, pp. 1-10, 03 07 2018.

[43] N. Chamanara, Y. Vahabzadeh and C. Caloz, "Simultaneous Control of the Spatial and Temporal Spectra of Light With Space-Time Varying Metasurfaces," *IEEE Transactions on Antennas and Propagation,* vol. 67, no. 4, pp. 2430-2441, 04 2019.

[44] C. N. Viswanathan, R. W. Longman and P. W. Likins, "A degree of controllability definition - Fundamental concepts and application to modal systems," *Journal of Guidance, Control, and Dynamics,* vol. 7, no. 2, pp. 222-230, 03 1984.

[45] J. D. Biggs and A. Negri, "Orbit-Attitude Control in a Circular Restricted Three-Body Problem Using Distributed Reflectivity Devices," *Journal of Guidance, Control, and Dynamics,* vol. 42, no. 12, pp. 2712-2721, 2019.

[46] R. S. Stansbury, *Local Search Algorithms,* Daytona Beach, FL, 2020.

[47] M. Whiting, "Destruction Junction - What's Your Function?," 6 August 2017. [Online]. Available: https://www.nasa.gov/feature/destruction-junction-what-s-your-function.

[48] "LightSail Flight by Light for CubeSats," [Online]. Available: https://www.planetary.org/explore/projects/lightsail-solar-sailing/.

[49] A. Tewari, "Adaptive Vectored Thrust Deorbiting of Space Debris," *Journal of Spacecraft and Rockets,* pp. 394-401, 2013.

[50] S. Gong and J. Li, "A new inclination cranking method for a flexible spinning solar sail," *IEEE Transactions on Aerospace and Electronic Systems,* vol. 51, no. 4, pp. 2680-2696, 2015.

[51] M. Polites, J. Kalmanson and D. Mangus, "Solar sail attitude control using small reaction wheels and magnetic torquers," *Journal of Aerospace Engineering, Part G,* vol. 222, no. G1, pp. 53-62, 2007.

[52] S. Gong and M. Macdonald, "Review on Solar Sail Technology," *Astrodynamics,* no. 3, pp. 93-125, 2019.

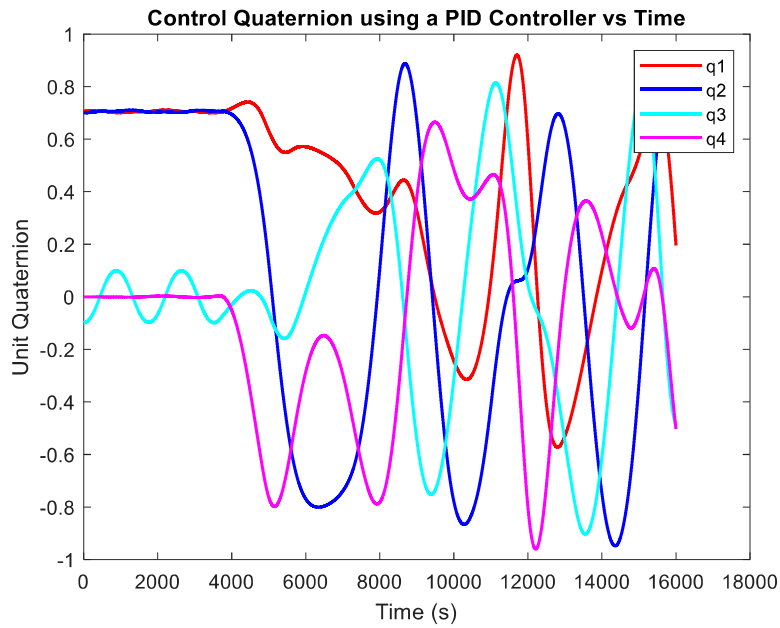**APPENDIX A**

State Response Graphs

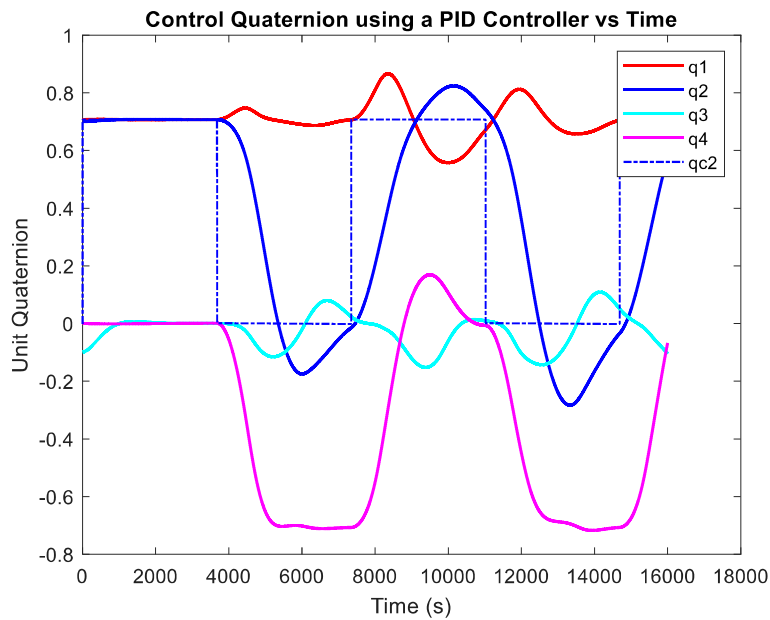*Figure A.1: State response used to find the Tc Zeigler-Nichols coefficient where Kcr=20 and umax= 0.5*10^-3*

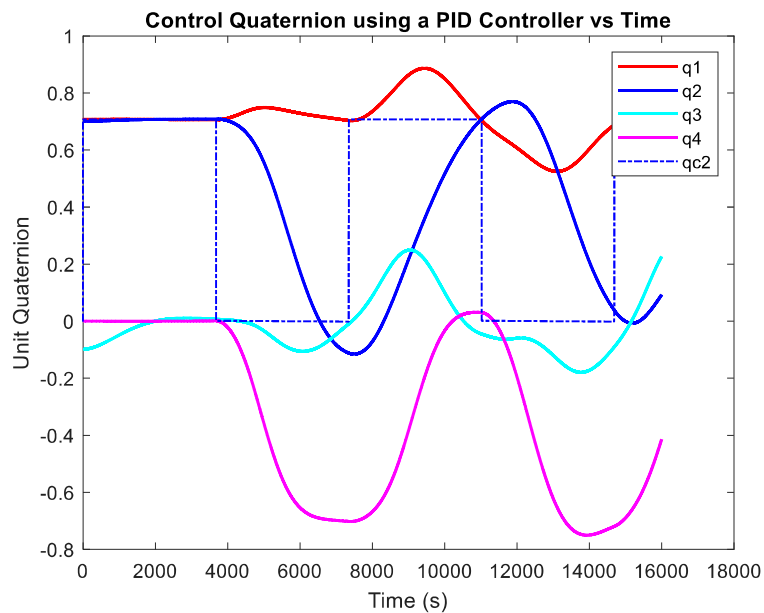*Figure A.2: State response using unaltered Zeigler Nichols derived PID gains for umax = 0.5*10^-3*

Figure A.3: State response using unaltered Zeigler Nichols derived PID gains for umax = 0.2mNm